

# Evidence for a bottom-light initial mass function in massive star clusters

H. Baumgardt<sup>1\*</sup>, V. Hénault-Brunet<sup>2</sup>, N. Dickson<sup>2</sup>, A. Sollima<sup>3†</sup>

<sup>1</sup> School of Mathematics and Physics, The University of Queensland, St. Lucia, QLD 4072, Australia

<sup>2</sup> Department of Astronomy and Physics, Saint Mary's University, 923 Robie Street, Halifax, NS B3H 3C3, Canada

<sup>3</sup> INAF Osservatorio Astronomico di Bologna, via Gobetti 93/3, Bologna, 40129, Italy

Accepted 2021 xx xx. Received 2021 xx xx; in original form 2021 xx xx

## ABSTRACT

We have determined stellar mass functions of 120 Milky Way globular clusters and massive LMC/SMC star clusters based on a comparison of archival Hubble Space Telescope photometry with a large grid of direct  $N$ -body simulations. We find a strong correlation of the global mass function slopes of star clusters with both their internal relaxation times as well as their lifetimes. Once dynamical effects are being accounted for, the mass functions of most star clusters are compatible with an initial mass function described by a broken power-law distribution  $N(m) \sim m^\alpha$  with break masses at  $0.4 M_\odot$  and  $1.0 M_\odot$  and mass function slopes of  $\alpha_{Low} = -0.3$  for stars with masses  $m < 0.4 M_\odot$ ,  $\alpha_{High} = -2.30$  for stars with  $m > 1.0 M_\odot$  and  $\alpha_{Med} = -1.65$  for intermediate-mass stars. Alternatively, a log-normal mass function with a characteristic mass  $\log M_C = -0.36$  and width  $\sigma_C = 0.28$  for low-mass stars and a power-law mass function for stars with  $m > 1 M_\odot$  also fits our data. We do not find a significant environmental dependency of the initial mass function with either cluster mass, density, global velocity dispersion or metallicity. Our results lead to a larger fraction of high-mass stars in globular clusters compared to canonical Kroupa/Chabrier mass functions, increasing the efficiency of self-enrichment in clusters and helping to alleviate the mass budget problem of multiple stellar populations in globular clusters. By comparing our results with direct  $N$ -body simulations we finally find that only simulations in which most black holes are ejected by natal birth kicks correctly reproduce the observed correlations.

**Key words:** globular clusters: general – stars: luminosity function, mass function

## 1 INTRODUCTION

The initial mass function (IMF) of stars is important in understanding a large number of astronomical phenomena such as the formation of the first stars (Bromm et al. 2009), galaxy formation and evolution (e.g. Calura & Menci 2009; Abe et al. 2021), and the determination of the absolute star formation rate (Aoyama, Ouchi & Harikane 2021). It also plays a dominant role in any star formation theory as the end result of molecular cloud contraction and fragmentation (e.g. Krumholz 2014).

The stellar IMF was first measured by Salpeter (1955), who found that the mass function of massive,  $m > 1 M_\odot$  stars in the solar neighborhood is best described by a power-law mass function  $N(m) \sim m^\alpha$  with slope  $\alpha = -2.35$ . Ev-

idence has been accumulating that the mass function for lower-mass stars in the Galactic disc increases less strongly with decreasing mass (Kroupa 2001; Chabrier 2003), but its exact form and whether it varies between individual star forming clouds is still under debate (see review by Bastian, Covey & Meyer 2010).

There has also been increasing evidence that the stellar mass function is varying with galaxy environment or cosmic time. The best possible case for IMF variations are probably the centers of early type galaxies, in which spectroscopic measurements (e.g. van Dokkum & Conroy 2010) as well as measurements of the stellar kinematics (Cappellari et al. 2012) indicate that the low-mass star IMF must be bottom-heavy. It has also been suggested that, due to inefficient cooling, the mass function of the first stars in the universe must have been top-heavy (Abel, Bryan & Norman 2002; Bromm, Coppi & Larson 2002). Top-heavy IMFs for high mass stars have also been found in massive Galactic

\* E-mail: h.baumgardt@uq.edu.au

† Deceased

molecular cloud complexes like W43 (Pouteau et al. 2022; Nony et al. 2023), which could indicate that the IMF slope depends on star formation rate and that starburst events create top-heavy IMFs. Finally, theoretical arguments and radiation-hydrodynamical simulations (e.g. Krumholz et al. 2010) indicate that radiation feedback from forming stars or cooling from dust-grains Chon, Omukai & Schneider (2021) could influence proto-stellar fragmentation and thereby the form of the IMF.

Star clusters are one of the best environments to determine the initial stellar mass functions since they offer large, statistical significant numbers of stars of similar distance, age and chemical composition. The strong crowding of stars in the cluster centres makes the detection of their lowest mass stars a challenge even when using space-based observatories like the Hubble Space Telescope (HST). In addition, the large angular extent of nearby star clusters means that it is usually not possible to obtain photometry of the whole cluster with a single HST pointing. It is therefore necessary to use models like multi-mass King-Michie models (Gunn & Griffin 1979; Sollima et al. 2017) that can correct for internal mass segregation in star clusters to correct locally measured mass functions to the global mass function. In addition, the dynamical evolution of star clusters needs to be taken into account when trying to deduce the initial mass function of a cluster from the present-day one since star clusters lose preferentially their lowest mass stars over time (Vesperini & Heggie 1997; Baumgardt & Makino 2003).

In this paper we determine the stellar mass functions of 120 Galactic globular clusters and Large and Small Magellanic cloud clusters from archival HST photometry, obtaining the largest database of mass function measurements for these systems. We then use this data to determine their initial mass functions and compare them to stellar mass functions measured for nearby galaxies. Our paper is organised as follows. In Sect. 2 we describe the selection of the clusters and the analysis of the HST data and in Sect. 3 we describe the determination of the stellar mass functions. In Sect. 4 we describe the results and we draw our conclusions in Sect. 5.

## 2 PHOTOMETRY

We took the input list of Milky Way globular clusters from the most recent version of the globular cluster database of Baumgardt et al. (2019), which lists 165 Galactic globular clusters. From this list we removed all clusters which either had no existing deep HST photometry reaching several magnitudes below the main sequence turn-over, were in fields of high stellar background density, or had large extinction values  $E(B-V) > 0.80$ . We also removed clusters for which the available HST photometry was not deep enough to allow us to determine the stellar mass function down to masses of at least  $\sim 0.50 M_{\odot}$ . In total we found 91 Galactic globular clusters which fulfilled all of the above constraints and we list these clusters in Table B1. In order to extend the measured mass functions to stars with masses above  $0.8 M_{\odot}$ , which have already turned into compact remnants in  $\sim 12$  Gyr old globular clusters, we also analysed stellar mass functions for 29 massive star clusters of the Large (LMC) and Small Magellanic Clouds (SMC) that have deep HST photometry and

we list the adopted parameters and derived mass function slopes of these clusters in Table B2.

For each star cluster we selected from the STSci data archive suitable HST photometry, making sure that we could get an as large as possible radial range for which we can measure the stellar mass function. Due to their proximity, this generally required us to analyse more than one HST field for Galactic globular clusters, while the more distant star clusters in the LMC and SMC usually fitted into a single HST field. Figs. A1 to A20 depict for each star cluster the location of the analysed HST fields.

After downloading the HST data, we prepared the photometric images using the `splitgroups` and camera-specific masking tasks as described in the DOLPHOT handbook and then performed stellar photometry on the data using DOLPHOT (Dolphin 2000, 2016). For ACS and WFC3 data, we performed the photometry on the CTE corrected flc images, while for the WFPC2 observations we used the c0m images to perform the photometry. We used the point-spread functions provided for each camera and filter combination by DOLPHOT for the photometric reductions. Photometry was done by using the drizzled drc and drz images provided by the STSci data archive as master frames, which also correct for geometric camera distortions. After obtaining the photometry, we removed detected objects that either had sharpness values  $|s| > 0.1$  or roundness parameters  $r$  larger than  $r > 0.25$  from the list of sources. The final magnitude and their associated errors for each star were calculated as the average and the r.m.s. of the individual magnitudes.

After performing the photometry, we cross-matched the HST coordinates of bright stars with the positions of stars in the *Gaia* DR3 catalogue (Gaia Collaboration et al. 2022) using the *Gaia* proper motions to move the *Gaia* positions from the 2016.0 *Gaia* DR3 epoch to the observation epoch of the HST data. We then applied position dependent shifts to the HST coordinates to bring them into agreement with the *Gaia* DR3 ones. These shifts were for each star calculated by determining the median shift of the nearest 30 stars against their *Gaia* DR3 counterparts. For clusters with a high stellar background density, and if more than one data set in a given field was available, we performed astrometry for multiple epochs this way and then determined individual proper motions for the stars. We then fitted a Gaussian mixture model to the resulting proper motion vector point diagram, modeling both the cluster and the background stars as two-dimensional Gaussians. From the fit we then calculated membership probabilities and selected as cluster stars all stars that had a probability larger than 10% to be cluster members. We chose this relatively low limit since we can remove most of the remaining non-members by the isochrone fits described further below. For clusters with significant stellar background density but only one available epoch, proper motion cleaning is not possible. In order to remove the contribution of non-members in these clusters, we shifted the best-fitting isochrone in colour and determined stellar number counts to the left and right of the cluster main sequence and in regions that are occupied only by background stars. We then averaged the resulting stellar numbers per magnitude interval and subtracted them from the stellar number counts for the cluster main sequence.

For clusters with significant and position dependent reddening we also de-reddened the final colour magnitude

diagrams (CMDs) before fitting the CMDs with stellar isochrones. Cluster de-reddening was done by first fitting an isochrone to the CMD of the central cluster parts. For each star we then calculated its displacement from this isochrone along the reddening vector. The coefficients of the reddening vector were calculated based on the analytic formulae of Cardelli, Clayton & Mathis (1989) assuming  $R(V) = 3.1$ . We also selected a magnitude interval where the CMD was dominated by cluster stars. We then corrected the CMD position of each star by calculating the mean displacement of the stars nearest to it. The number of stars used and the magnitude limits were varied for each cluster depending on the total number of cluster stars and the strength of the background contamination. Fig. 1 shows as an example the effects of proper motion cleaning and de-reddening for the globular cluster NGC 6558.

For each analysed HST field we also estimated the photometric completeness using artificial star tests. To this end, we distributed artificial stars with uniform spatial density across each HST field. Stars were equally spread in magnitude along the location of each cluster’s main sequence from the turnover down to the faintest detectable magnitudes. We created 100,000 artificial stars in HST fields that covered cluster centres and 25,000 stars for HST fields that covered areas outside the centre. We used a larger number of stars for central fields since these are more affected by crowding and the completeness fraction will vary more quickly with radius since the stellar density varies strongly with radius in the centre. We used the DOLPHOT `fakestars` task to recover the magnitudes of the artificial stars and applied the same quality cuts to the artificial stars that we used to select real stars in the observed data sets. We then estimated the completeness fraction for each observed star from the ratio of successfully recovered stars to all inserted stars using the nearest 20 artificial stars that are within 0.2 mag of the magnitude of each observed star. In order to limit the influence of photometric incompleteness, we analysed mass functions only down to magnitudes where the average completeness is above 75% in each field. The only exception were WFPC2 observations where DOLPHOT seemed to have problems in properly aligning the individual data frames to the drizzled `drz` master frames and in which the photometric completeness was typically only around 75% even for bright, non-saturated stars. Since the alignment problems do not seem to depend on the stellar magnitudes and the completeness tests seem to be able to correct for their effect, we adopted a smaller completeness limit of 50% for WFPC2 data.

### 3 MASS FUNCTION DETERMINATION

#### 3.1 Isochrone fits

We determined stellar mass functions by performing isochrone fits to the observed CMDs. In order to determine the best-fitting isochrone, we varied the assumed cluster distances and reddenings but took the cluster ages and metallicities for which the isochrones were generated from literature data. We took the ages mainly from the compilations of De Angeli et al. (2005), Marín-Franch et al. (2009), Dotter et al. (2010), VandenBerg et al. (2013) and Valcin et al.

(2020). In order to account for systematic differences between the ages derived in these papers, we first averaged all ages and then calculated shifts for each individual paper against the mean ages determined this way. For the comparison we allowed the shifts to depend linearly on metallicity. This assumption is compatible with the observed age differences between different studies, see e.g. Fig. 9 in (Marín-Franch et al. 2009). After correcting systematic differences in this way, we then calculated a final average age of each cluster. We took the cluster metallicities from the compilation of Carretta et al. (2009). We then created DSEP isochrones (Dotter et al. 2008) with these metallicities and ages and fitted the isochrones to the cluster CMDs. We used DSEP isochrones with an  $\alpha$  element abundance enhancement of  $\alpha = 0.2$  for clusters with  $[\text{Fe}/\text{H}] < -1.0$  and solar composition for clusters with metallicities larger than  $[\text{Fe}/\text{H}] = -1.0$ . To test the influence of the choice of isochrones on our results, we also fitted PARSEC isochrones (Bressan et al. 2012; Chen et al. 2014, 2015) to the clusters, but found that the derived global mass function slopes changed by less than  $\Delta\alpha = 0.20$  dex.

In order to fit the isochrones, we took the initial values of the cluster reddening from Harris (1996) and the cluster distances from Baumgardt & Vasiliev (2021). We then varied reddening and distance until we achieved the best fit to each observed CMD. Table B1 gives the best-fitting reddenings and distances for each cluster, averaged over all individual CMDs that we fitted for each cluster. The resulting reddening and distance values are usually within  $\pm 0.05$  mag of the reddening given by Harris (1996) and within  $\pm 0.10$  in distance modulus to the distances from Baumgardt & Vasiliev (2021). Once the best-fitting isochrones had been determined, we selected all stars with photometry compatible with each isochrone in radial annuli of  $20''$  width. We also calculated a best-fitting power-law mass function slope  $N(m) \sim m^\alpha$  for each radial annulus using the maximum likelihood method described in Clauset, Shalizi & Newman (2009) and Khalaj & Baumgardt (2013), which uses unbinned data. We note that our final results are rather insensitive to the assumed ages and metallicities, the measured mass function slope changes for example by only about 0.10 dex for a change in cluster age of 1 Gyr or a change in metallicity by  $\Delta[\text{Fe}/\text{H}] = 0.20$ .

## 4 RESULTS

### 4.1 Initial mass function of clusters

In this section we derive the mass function of star clusters that have relaxation times  $T_{RH}$  of the order of their ages and total lifetimes at least three times larger than their ages. These clusters should have largely preserved their mass functions since they lost only a small fraction of their mass. In addition, due to their large relaxation times such clusters are also not strongly mass segregated and therefore even the small amount of mass loss they have experienced will lead to a loss of stars independent of their masses (at least as long as the clusters started without primordial mass segregation). We therefore assume that the present-day mass functions of these clusters resemble their initial mass functions. These assumptions are confirmed by the results of the

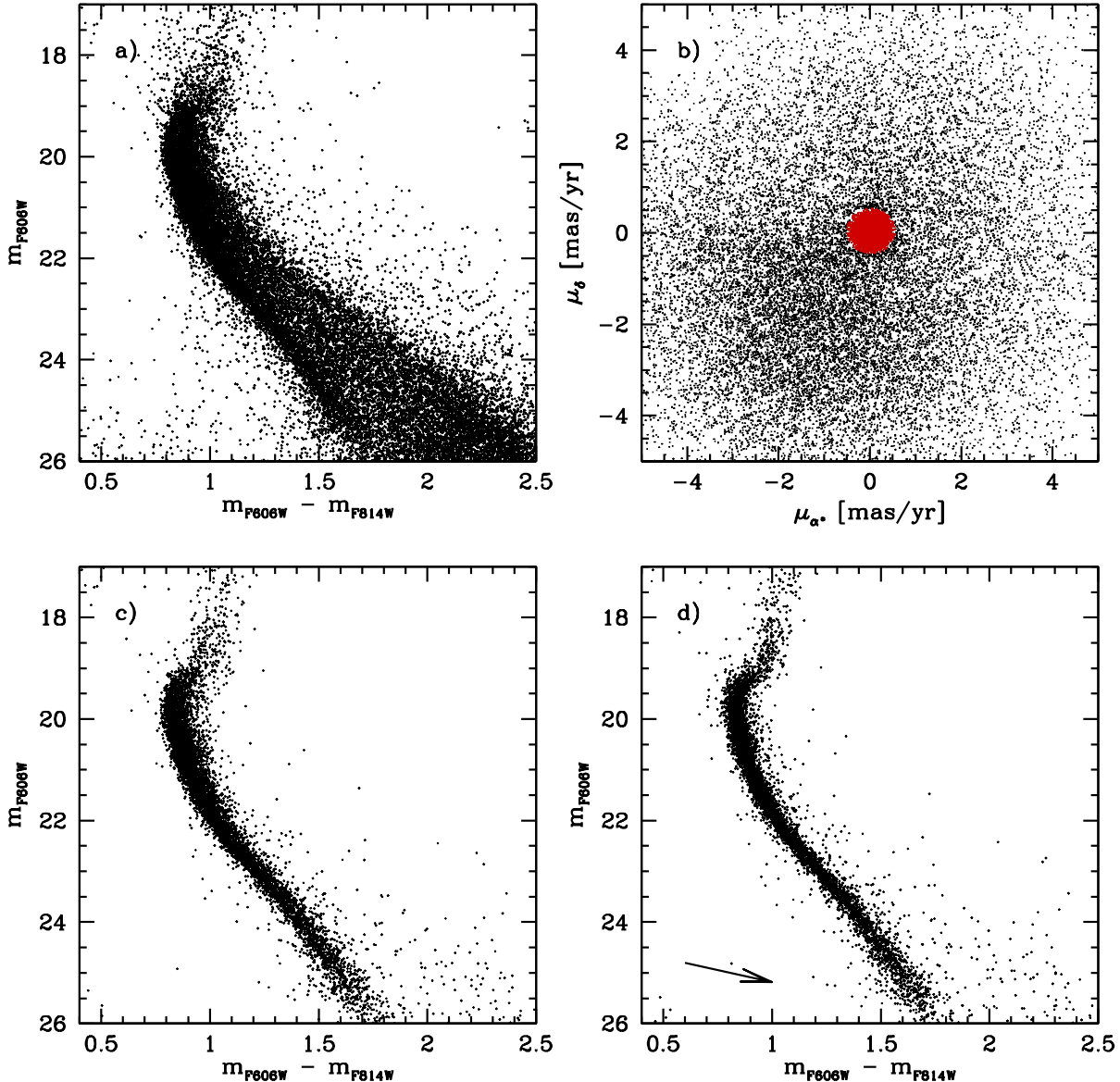


**Figure 1.** Example showing the effects of proper motion cleaning and differential reddening correction on the observed CMD of NGC 6558. Panel a) shows an  $m_{F606W} - m_{F814W}$  vs.  $m_{F606W}$  colour-magnitude diagram of all stars that pass the sharpness and roundness criteria. Panel b) shows the proper-motion vector point diagram of these stars with the cluster centered at the origin. Stars marked in red are stars that pass the proper motion membership test. Panel c) shows the CMD after stars with membership probabilities less than 10% have been removed. Panel d) shows the CMD of the member stars after differential reddening correction, which leads to a further narrowing of the CMD. The arrow in the bottom right panel shows the direction of the reddening vector.

$N$ -body simulations done in sec. 4.2 of this paper as well as by the  $N$ -body simulations done by Webb & Leigh (2015). We derive the mass function for stars with masses  $m < 0.8 M_{\odot}$  from Milky Way globular clusters and the mass function of higher mass stars from the LMC and SMC star clusters.

#### 4.1.1 The low-mass star IMF

In this section we restrict ourselves to globular clusters that have mass function determinations both inside and outside their half-mass radii and for which the mass functions can be determined down to at least  $m = 0.25 M_{\odot}$ . This way we can measure the mass function directly from the observations and are independent of model fits. These requirements

restrict us to six globular clusters: IC 4499, NGC 5024, NGC 5053, NGC 5139, NGC 6101 and Ter 8.

For each cluster we use the method described in Baumgardt et al. (2022) to determine the fraction  $f_r$  of the cluster that is covered by our photometry at the projected distance of each star from the centre. We then assign a weighting factor  $w = 1/(f_r f_p)$  to each star where  $f_p$  is the fraction of stars of similar magnitudes and location that are recovered in our completeness tests. For NGC 5024 and NGC 5139 we are not able to apply this procedure to the innermost parts since our photometry becomes incomplete at masses  $m \sim 0.5 M_{\odot}$  due to crowding. The derived mass functions for these clusters could therefore be slightly skewed towards lower masses as we tend to miss preferentially higher mass

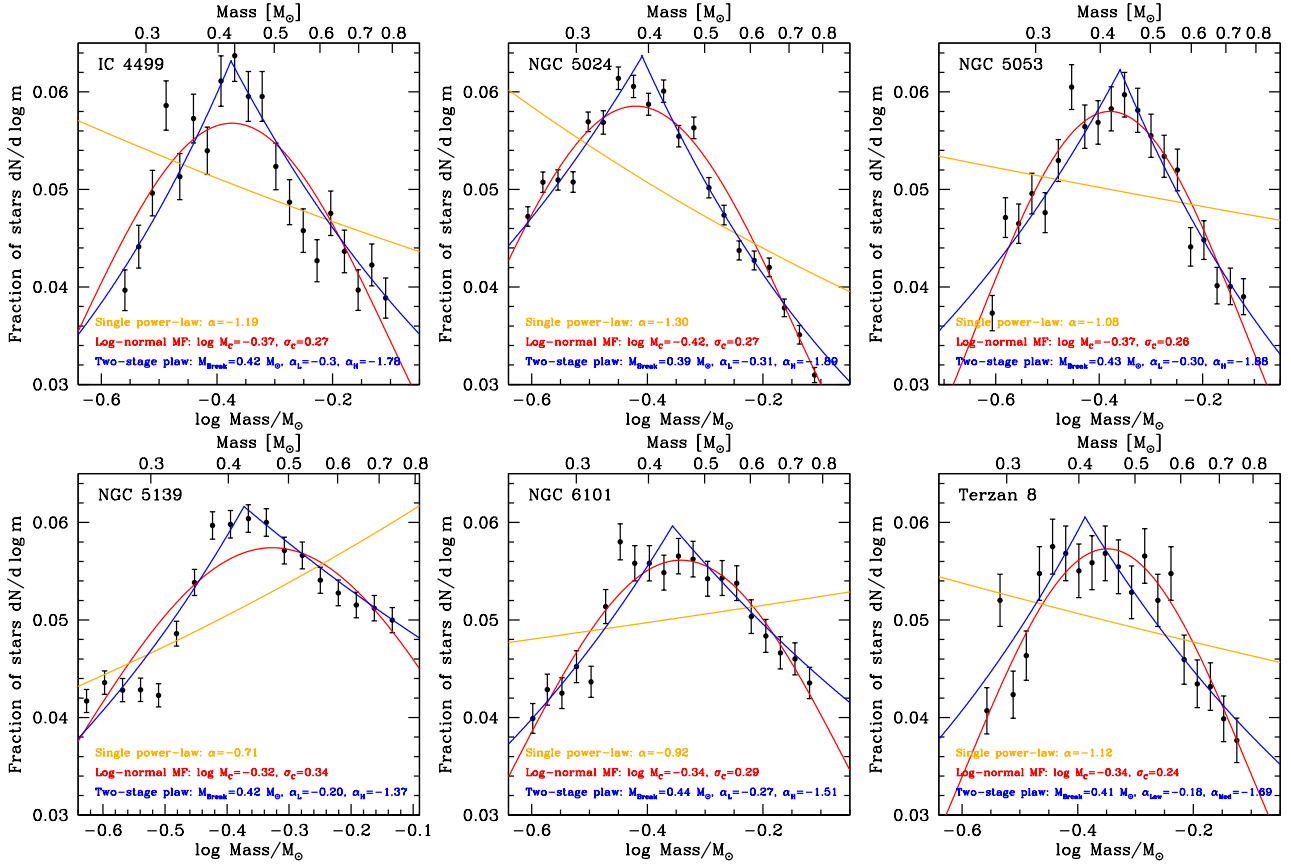


**Figure 2.** Global mass functions for (clockwise from top left) IC 4499, NGC 5024, NGC 5053, Ter 8, NGC 6101 and NGC 5139, the six globular clusters in our sample that have both large relaxation and lifetimes and photometry deep enough to reach down to at least  $0.25 M_\odot$ . Filled black circles with error bars show the fraction of observed stars as a function of mass in the different clusters and their  $1\sigma$  errors. The orange, blue and red lines show fits of the best-fitting single power law, two-stage power law and log-normal mass functions to the data. The parameter of the fits are given in each panel. There is generally quite good agreement between the parameters that we find for each cluster, implying that all clusters have started with very similar mass functions. A two-stage power-law and a log-normal mass function provide about equally good fits to the data, while a single power-law mass function overpredicts the number of high and low-mass stars and underpredicts the number of stars with masses around  $0.4 M_\odot$ . The deviations are however only of order 10%.

stars due to mass segregation. However the effect is likely only small since we are analysing clusters with large relaxation times which are not strongly mass segregated. We similarly lose a few percent of the outermost stars in all clusters since our photometry does not reach the tidal radius, however we again expect that this is not going to have a strong effect on our results.

After deriving the individual stellar masses, we then fit a single-power mass function, a two-stage power-law mass function with a break-mass  $m_{Break}$  and a mass function slope  $\alpha_{Med}$  for stars with  $m > m_{Break}$  and a low-mass slope  $\alpha_{Low}$  for stars with  $m < m_{Break}$ , and a log-normal mass function  $\phi(m) \sim e^{-(\log M_C - \log m)^2 / (2\sigma_C^2)}$  with a characteristic mass  $M_C$  and a width  $\sigma_C$  to the data. We derive the best-fitting parameters for each of these models using a maximum-likelihood approach, following the procedure outlined by Clauset, Shalizi & Newman (2009). Fig. 2 depicts the mass distribution of stars in each of the six clusters as well as the results of our fits. It can be seen that single power-law mass functions are not accurate fits to the data since they predict too many high and low-mass stars and too few intermediate stars with masses around  $0.4 M_\odot$ . However, the

relative deviations from the actual data are for most masses only of order 10%, so a single power-law mass function is still a useful approximation. Fig. 2 also shows that two-stage power-law mass functions and log-normal mass functions provide significantly better fits to the data. For a two-stage power-law mass function, we obtain break masses  $m_{Break}$  between  $0.39 M_\odot$  to  $0.44 M_\odot$ , mass function slopes between  $\alpha_M \approx -1.40$  to  $\alpha_M \approx -1.90$  for stars more massive than the break mass and significantly flatter mass function slopes for the low-mass stars. The mass function does therefore flatten towards lower masses, a behavior qualitatively similar to that seen for Galactic disc stars (Kroupa 2001). The individual slopes are however flatter at all masses, leading again to a mass function with a smaller fraction of low-mass stars compared to what is found in the Galactic field. Taking the average over all six clusters we obtain for the break mass, and the high and low-mass slopes:  $m_{Break} = 0.42 \pm 0.02$ ,  $\alpha_{Med} = -1.68 \pm 0.20$  and  $\alpha_{Low} = -0.27 \pm 0.08$ . Here the error bars reflect the standard deviation of the individual clusters around the mean. We decided to use the standard deviation as an estimate of the uncertainty since the formal error bars are usually small (typically of order 0.02) and do

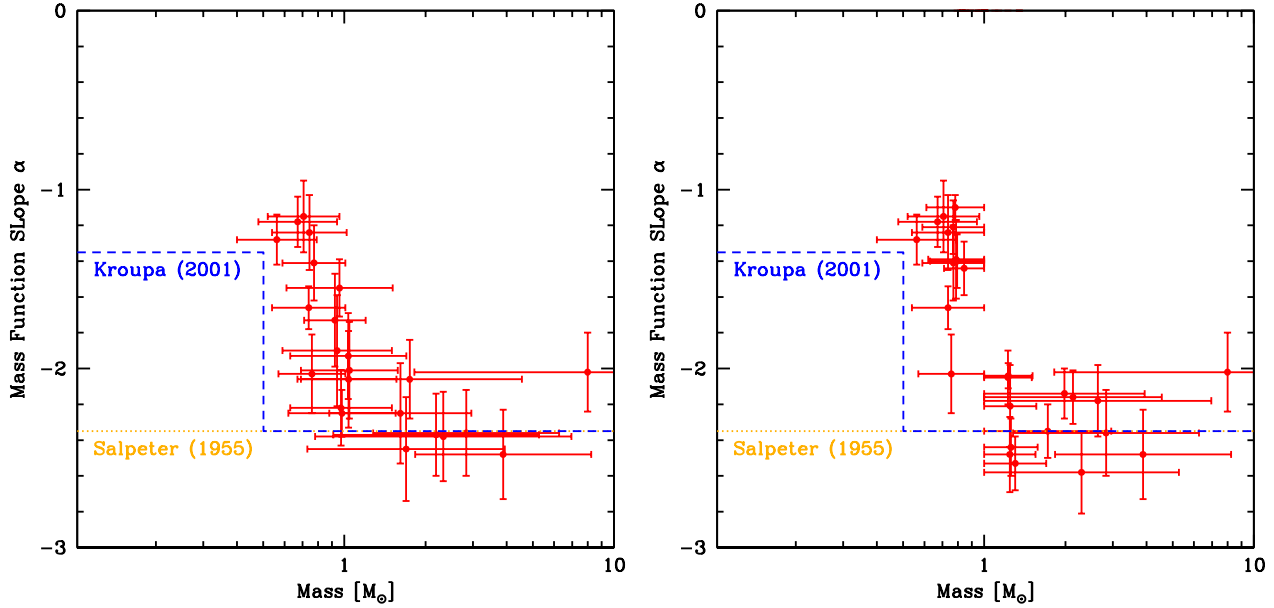


**Figure 3.** Mass function slopes for massive LMC and SMC star clusters. Horizontal lines depict the mass range for which the mass functions have been determined, vertical lines depict the uncertainty in the derived mass function slopes. In the left panel we show the slopes derived over the full mass range that could be fitted in each cluster, while in the right panel we have split the sample into two mass ranges for stars less and more massive than  $1 M_{\odot}$ . There seems to be a clear break in mass function slope at around  $1 M_{\odot}$ .

not reflect systematic errors which, under the assumption of a common initial mass function, should be better represented by the standard deviation.

Fig. 2 also shows that log-normal mass functions provide acceptable fits to the data. The values that we derive for the parameters are again similar between the different clusters, making it possible that all clusters have started with the same mass function. Taking an average over all clusters, we find  $\log M_C = -0.36 \pm 0.03$  and  $\sigma_C = 0.28 \pm 0.04$ . The Chabrier (2003) mass function, which fits the distribution of stars in the Galactic disc, has a characteristic mass of  $\log M_C = -1.00$ . Hence our results again argue for a smaller fraction of low-mass stars in globular clusters compared to the Galactic disc.

#### 4.1.2 The high-mass star IMF

Since globular clusters only allow to determine the sub-solar stellar mass function, we next extend our analysis to the stellar mass functions of a number of massive star clusters in the LMC/SMC that have available deep HST photometry. The chosen clusters span a range of ages between 3 Myr and 12 Gyr and have masses from about  $10^4 M_{\odot}$  to  $7 \cdot 10^5 M_{\odot}$ , similar to the masses of the globular clusters studied previously. We analyse each LMC/SMC star cluster in the same way as the Milky Way globular clusters by deriving their photometry from HST observations. Due to the large distances of the LMC and SMC, a single HST field is usually sufficient to cover most stars in a star cluster. From a comparison of the available observational data of each cluster to a grid of  $N$ -body simulations (to be described below), we then derive the physical parameters of the clusters including their mass functions. The basic data of the clusters (distances, ages, extinctions) are taken from Milone et al. (2023), or, for clusters

not studied in this paper from available literature. We take the lifetimes of the clusters from Baumgardt et al. (2013), who determined lifetimes assuming that the clusters move in circular cluster orbits around the center of their parent galaxy. This seems to be a good approximation at least for the star clusters of the LMC (Bennet et al. 2022). Table B2 gives the parameters adopted in the fitting of the cluster CMDs together with the derived mass function slopes.

The lifetimes and relaxation times of the LMC/SMC clusters are generally larger than their cluster ages, hence we do not expect the stellar mass function of these clusters to have significantly changed since their formation. Fig. 3 shows the derived mass function slopes for the LMC/SMC star clusters. The left panel depicts the slopes derived for the full range of stellar masses that we can fit. It can be seen that there is a gradual change of the stellar mass function around  $1 M_{\odot}$ . High-mass stars with masses  $m > 1 M_{\odot}$  have slopes close to a Salpeter mass function ( $\alpha = -2.3$ ) while for low-mass stars the average power-law slope is around  $\alpha \approx -1.4$ . The transition between both slopes happens at a mass of about  $m = 1 M_{\odot}$ . This conclusion is strengthened by the right panel in Fig. 3, where we have determined mass functions separately for stars with masses below and above  $1 M_{\odot}$ . We have restricted the fits in this panel to clusters where either the low-mass limit is below  $0.60 M_{\odot}$  or the high-mass limit is above  $1.60 M_{\odot}$ . It can be seen that the derived slopes split into two well separated groups. The high-mass star function is compatible with a Salpeter slope with  $\alpha = -2.3$  in essentially all clusters, while the low-mass stellar mass function has an average slope of  $\alpha \approx -1.4$ , compatible with what we found for Galactic globular clusters.

Combining the Milky Way and LMC/SMC results, and assuming that the Milky Way GCs had a high-mass star mass function similar to the LMC/SMC clusters, we can

**Table 1.** Details of the performed  $N$ -body simulations of star clusters evolving in tidal fields. Columns 3 and 4 contain the initial cluster mass and half-mass radius. Column 5 contains the assumed black hole retention fraction. Columns 6 and 7 contain the semi-major axis and eccentricity of the cluster orbits. Column 8 contains the remaining mass fraction at  $T = 13.5$  Gyr and column 9 the estimated lifetimes of the clusters.

Model	$N_{Stars}$	$M_{Ini}$ [ $M_{\odot}$ ]	$r_{h,Ini}$ [pc]	$f_{BH}$	$a_{Orb}$ [pc]	$e_{Orb}$	$M_{Fin}/M_{Ini}$	$T_{Diss}$ [Gyr]
1	70,000	$7.0 \cdot 10^5$	3.0	0.10	10000	0.00	0.197	21.7
2	70,000	$7.0 \cdot 10^5$	3.0	0.10	5000	0.00	0.000	12.9
3	70,000	$7.0 \cdot 10^5$	3.0	0.10	7500	0.00	0.104	16.4
4	70,000	$7.0 \cdot 10^5$	2.0	0.10	6500	0.50	0.000	12.4
5	70,000	$7.0 \cdot 10^5$	3.0	0.10	15000	0.00	0.294	34.4
6	70,000	$7.0 \cdot 10^5$	5.0	0.10	15000	0.00	0.231	26.1
7	70,000	$7.0 \cdot 10^5$	3.0	0.10	20000	0.00	0.340	48.9
8	70,000	$7.0 \cdot 10^5$	5.0	0.10	20000	0.00	0.296	37.3
9	131,000	$1.3 \cdot 10^5$	3.0	0.10	5000	0.00	0.159	19.0
10	131,000	$1.3 \cdot 10^5$	2.0	0.10	6500	0.50	0.087	15.7
11	131,000	$1.3 \cdot 10^5$	2.0	0.10	6300	0.60	0.044	14.4
12	131,000	$1.3 \cdot 10^5$	3.0	0.10	10000	0.00	0.296	36.4
13	131,000	$1.3 \cdot 10^5$	5.0	0.10	14000	0.44	0.219	24.7
14	131,000	$1.3 \cdot 10^5$	3.0	0.10	3000	0.00	0.000	13.1
15	131,000	$1.3 \cdot 10^5$	5.0	0.10	7500	0.00	0.054	14.1
16	131,000	$1.3 \cdot 10^5$	5.0	0.10	10000	0.00	0.285	30.3
17	131,000	$1.3 \cdot 10^5$	5.0	0.10	11250	0.33	0.245	26.5
18	131,000	$1.3 \cdot 10^5$	5.0	0.10	20000	0.00	0.277	29.7
19	200,000	$2.0 \cdot 10^5$	3.0	0.10	3000	0.00	0.021	13.8
20	300,000	$3.0 \cdot 10^5$	3.0	0.10	3000	0.00	0.177	19.4

therefore describe the initial mass function of the clusters in our sample as a three-stage power-law with:

$$\begin{aligned} \alpha_{High} &= -2.30 \pm 0.15 \quad \text{for } m > 1 M_{\odot} \\ \alpha_{Med} &= -1.65 \pm 0.20 \quad \text{for } 0.4 M_{\odot} < m < 1 M_{\odot} \\ \alpha_{Low} &= -0.30 \pm 0.20 \quad \text{for } m < 0.4 M_{\odot} \end{aligned}$$

Alternatively, the initial mass function can also be described as a log-normal mass function with  $\log M_C = -0.36$  and  $\sigma_C = 0.28$  for stars with masses  $m < 1 M_{\odot}$  followed by a power-law mass functions for higher mass stars with a slope  $\alpha = -2.3$ .

#### 4.2 $N$ -body simulations of star cluster evolution

Having determined the initial cluster mass function from the dynamically least evolved clusters, we now turn our attention to fitting the full cluster sample. In order to do this, we first ran  $N$ -body simulations of star clusters dissolving in tidal fields starting from the three-stage power-law mass function determined in sec. 4.1. We will use these simulations in the next sections to determine the mass functions of evolved star clusters as well as to derive constraints on the black hole retention fraction of star clusters.

In total we ran 20  $N$ -body simulations of star clusters using NBODY7 (Nitadori & Aarseth 2012). The clusters contained between 70,000 to 300,000 stars initially and moved in either circular or elliptic orbits through an isothermal galaxy with a constant circular velocity of  $v_c = 240$  km/sec. The clusters followed King (1966) density profiles with dimensionless concentration parameter  $c = 1.5$  initially. We ran the simulations with an assumed neutron star and black hole retention fraction of 10%, i.e. 90% of the formed black holes and neutron stars were given large velocity kicks upon their formation so that they left their parent clusters. The retention fraction was applied to every formed neutron

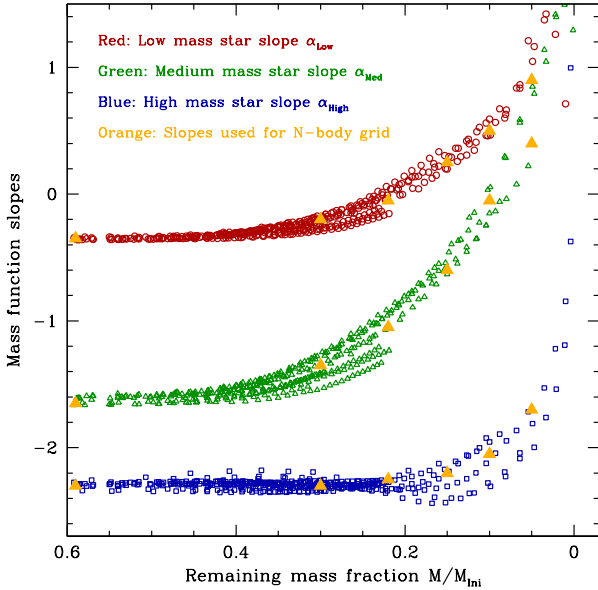
star and black hole independent of its mass. We took snapshots spaced by 500 Myr during the simulations and use the snapshots between 8 and 13.5 Gyr to determine the mass function of the remaining stars. By 13.5 Gyr, the studied clusters had lost between 20% to 100% of their initial stars. Table 1 gives details of the performed  $N$ -body simulations.

Fig. 4 depicts the change in the mass function slopes for low, intermediate-mass and high mass stars in the  $N$ -body simulations as a function of the mass lost in the clusters. We depict only the evolution starting from the point when the clusters contain 60% of their initial mass since the mass lost up to that point is mainly due to stellar evolution within the first Gyr of evolution. When deriving the mass function slopes, we used for all stars their initial masses in order to remove the effect of stellar evolution of massive stars on the mass function. For the same reason we fit only the mass range from 1.0 to 8.0  $M_{\odot}$  for the high-mass stars since most of the more massive stars were removed by natal velocity kicks, creating a discontinuity in the mass function. It can be seen that the clusters become increasingly depleted in low-mass stars as time progresses. The evolution is particularly strong for intermediate-mass stars ( $0.40 M_{\odot} < m < 1.0 M_{\odot}$ ) and towards the later stages of evolution. The slower mass function evolution in the beginning is most likely due to the fact that clusters first need to become mass segregated before significant changes occur to their internal mass functions. Overall the mass function evolution proceeds in a very similar way in the different clusters despite the fact that the simulations span a wide parameter range. Hence it can be expected that the evolution of real star clusters proceeds along a similar path.

The orange triangles in Fig. 4 mark the points when we determine (averaged) mass function slopes from the  $N$ -body simulations. We list the derived mass function values in Table 2. From the initial masses of the remaining neutron

**Table 2.** Power-law mass function slopes  $N(m) \sim m^\alpha$  and mass limits used as input values for our grid of  $N$ -body simulations.

Model	$M(t)/M_0$	$m_{Low}$ [ $M_\odot$ ]	$m_{Up}$ [ $M_\odot$ ]	$\alpha$	$m_{Low}$ [ $M_\odot$ ]	$m_{Up}$ [ $M_\odot$ ]	$\alpha$	$m_{Low}$ [ $M_\odot$ ]	$m_{Up}$ [ $M_\odot$ ]	$\alpha$	$m_{Low}$ [ $M_\odot$ ]	$m_{Up}$ [ $M_\odot$ ]	$\alpha$
1	1.00	0.10	0.40	-0.35	0.40	1.00	-1.65	1.00	6.50	-2.30	6.50	100.0	-2.30
2	0.30	0.10	0.40	-0.20	0.40	1.00	-1.35	1.00	6.50	-2.25	6.50	100.0	-2.80
3	0.22	0.10	0.40	-0.05	0.40	1.00	-1.05	1.00	6.50	-2.25	6.50	100.0	-3.15
4	0.15	0.10	0.40	0.25	0.40	1.00	-0.65	1.00	6.50	-2.20	6.50	100.0	-3.20
5	0.10	0.10	0.40	0.50	0.40	1.00	-0.05	1.00	6.50	-1.90	6.50	100.0	-3.20
6	0.05	0.10	0.40	0.80	0.40	1.00	0.30	1.00	6.50	-1.60	6.50	100.0	-3.80

**Figure 4.** Evolution of the mass function slopes  $\alpha$  of low (open circles), intermediate-mass (green triangles) and high-mass (blue squares) stars in the  $N$ -body simulations as a function of the remaining mass fraction  $M/M_{ini}$ . For all three mass groups the mass functions evolve towards positive values due to mass segregation and the preferential loss of lower mass stars. The evolution is stronger towards the final stages of cluster evolution and for the intermediate-mass stars. Orange triangles mark the mass function values that are given in Table 2 and that are used for the grid of  $N$ -body simulations described in sec. 4.3.

stars and black holes we also derive an additional slope for the highest mass stars. The derived values are somewhat uncertain due to the small number of remaining stars in the clusters. Nevertheless they show the strong depletion of the more massive black holes through dynamical encounters and binary formation in the cluster cores, which leads to a strong steepening of the mass function of the remaining black holes.

### 4.3 Derivation of the global mass function

The derivation of the global mass functions for clusters that are dynamically evolved and have incomplete spatial coverage from the HST photometry was done similar to Baumgardt (2017) and Baumgardt & Hilker (2018) by fitting a large grid of  $N$ -body models to each observed cluster and finding the model that best fits all available data for each cluster. We give a brief summary of this fitting procedure below, more details can be found in Baumgardt (2017) and Baumgardt & Hilker (2018).

We first used the six sets of mass function values listed in Tab. 2 and ran a large grid of  $N$ -body simulations using these values. For each mass function, we used eight values for the initial half-mass radius  $r_h$ , spaced roughly evenly in  $\log r_h$  between 2 pc and 35 pc and six values for the initial concentration index  $c$  of the initial King (1962) density profile between  $c = 0.2$  to  $c = 2.5$ . All  $N$ -body simulations were isolated simulations having  $10^5$  stars initially and were run for 13.5 Gyr. Like in the simulations in the preceding section, we assumed a 10% retention fraction of black holes and neutron stars in these models.

The fitting of the Galactic globular clusters and LMC/SMC star clusters was then done by selecting the snapshot closest in time to the age of an observed cluster from each  $N$ -body simulation and by then fitting these snapshots to the observational data available for each cluster. We scaled each  $N$ -body model along lines of constant relaxation time  $T_{RH}$  to the same half-light radius of an observed cluster, using the cluster distances that were derived by Baumgardt & Vasiliev (2021) by combining a variety of individual distance determinations. We then calculated the velocity dispersion and surface density profiles for each  $N$ -body model from the distribution of its bright stars. We also calculated a sky projection of each  $N$ -body model centered around the position of each observed cluster and selected stars from the  $N$ -body models that are in the same region of the sky as the observed HST fields. We then derived stellar mass function slopes for these regions and for the same radial annuli for which we have observational data.

We then interpolated in our grid of models and derived the model that provides the best fit to the observed surface density profile from Baumgardt, Sollima & Hilker (2020), the observed velocity dispersion profile, and to the observed mass function slopes at different radii that we calculated in this paper. We determine the best-fitting  $N$ -body model through  $\chi^2$  minimization against the observed data and adopt as best-fitting cluster parameters the parameters of this model. From the models with  $\chi^2 < \chi^2_{min} + 1$  we also obtain error bars on the cluster parameters. In order to reflect the influence that e.g. uncertainties in the cluster ages have on the derived mass functions slopes, we add an uncertainty of  $\Delta\alpha = 0.10$  in quadrature to the global mass function errors derived this way and adopt the resulting value as the final error.

In order to improve the accuracy with which we can reproduce the cluster parameters, we added kinematic data published in recent years to the kinematic data from Baumgardt & Hilker (2018). Most of this data comes from large scale radial velocity surveys targeting Milky Way stars like Gaia DR3 (Gaia Collaboration et al. 2022; Katz et al. 2022), Apogee DR17 (Abdurro'uf et al. 2022), Lamost DR7 (Cui

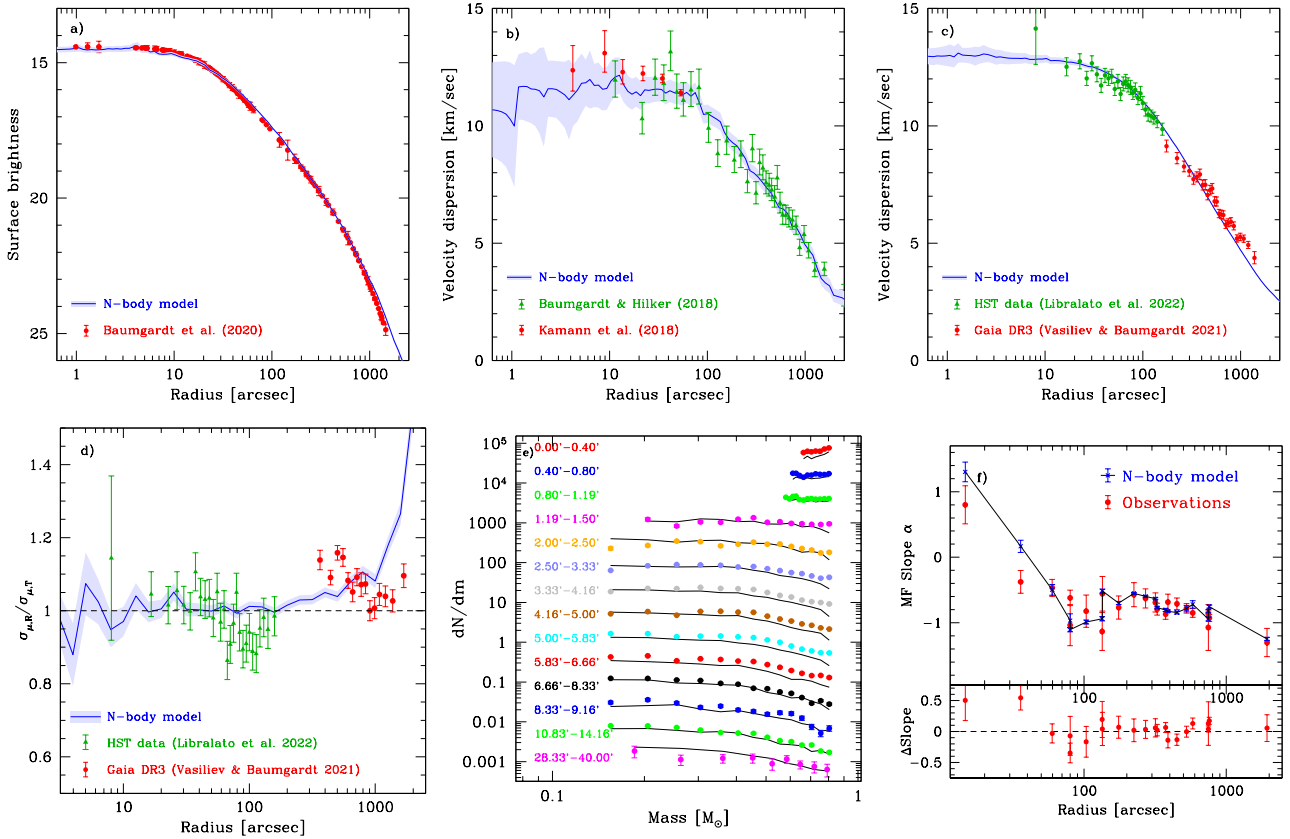


**Figure 5.** Comparison of the best-fitting  $N$ -body model to the observed surface density profile (panel a), line-of-sight velocity dispersion profile (panel b), proper motion velocity dispersion profile (panel c) velocity anisotropy profile (panel d), individual stellar mass functions at different radii (panel e) and the slope of the mass function as a function of radius (panel f) for the globular cluster NGC 104. It can be seen that the  $N$ -body model is in general in good agreement with the observations.

et al. 2012), Galah DR3 (Buder et al. 2021) and the WAGGS survey (Dalglish et al. 2020). We list additional sources improving kinematic data for particular clusters in the Appendix. From our fits we not only derived the stellar mass functions but also a range of other cluster parameters including total masses, core and half-mass radii and relaxation times  $T_{RH}$ , which we will use further below. Fig. 5 shows as an example of the fitting procedure our fit for the cluster NGC 104. It can be seen that our best-fitting  $N$ -body model reproduces the surface density and velocity dispersion profiles as well as the individual mass functions at various radii fairly well, despite the fact that our models need to fit a large amount of observational data with only few free parameters. We make the full set of comparisons as well as the derived parameters available on a dedicated website<sup>1</sup>. Finally, we also calculated the dissolution time  $T_{Diss}$  for each cluster using the approach described in sec. 3.2 of Baumgardt et al. (2019).

We present the derived mass function slopes in Tables B1 and B2. In these tables we have characterised the mass functions by both single power-law mass functions  $N(m) \sim m^{\alpha}$  over the whole observed mass range, as well as by two-stage power-law mass functions for clusters that have a sufficiently wide mass coverage to allow low-mass/high-

mass stars to be fitted separately. For the two-stage power-law mass functions we assumed fixed break masses of  $0.4 M_{\odot}$  (Milky Way GCs) and  $1.0 M_{\odot}$  (LMC/SMC clusters). In general two-stage power-law mass functions provide significantly better fits and we will therefore mostly use these in the rest of the paper.

Fig. 6 compares the mass function slopes that we find in this work with mass function determinations of Galactic globular clusters by De Marchi, Paresce & Pulone (2007), Paust et al. (2010), Ebrahimi et al. (2020) and Dickson et al. (2023) for the clusters in common. The first three papers characterised the stellar mass function by a single power-law slope  $N(m) \sim m^{\alpha}$  over the whole range of masses fitted. We therefore also use our single power-law mass function fits for comparison. It can be seen that the mass function slopes determined by De Marchi, Paresce & Pulone (2007) and Paust et al. (2010) span a larger range in values compared to our data and are also lower on average. This could at least partly be due to the fact that their lower-mass limits are usually higher, causing their mass functions to be more strongly dominated by stars with masses  $m > 0.4 M_{\odot}$  which have a steeper mass function slope. Some of the mass function slopes quoted by De Marchi, Paresce & Pulone (2007) are also locally measured ones that were not corrected for mass segregation. This will lead to an under or over estimation of the global mass function slopes if the local mass function was determined in the cluster centre or the cluster halo. We

<sup>1</sup> <https://people.smp.uq.edu.au/HolgerBaumgardt/globular/>

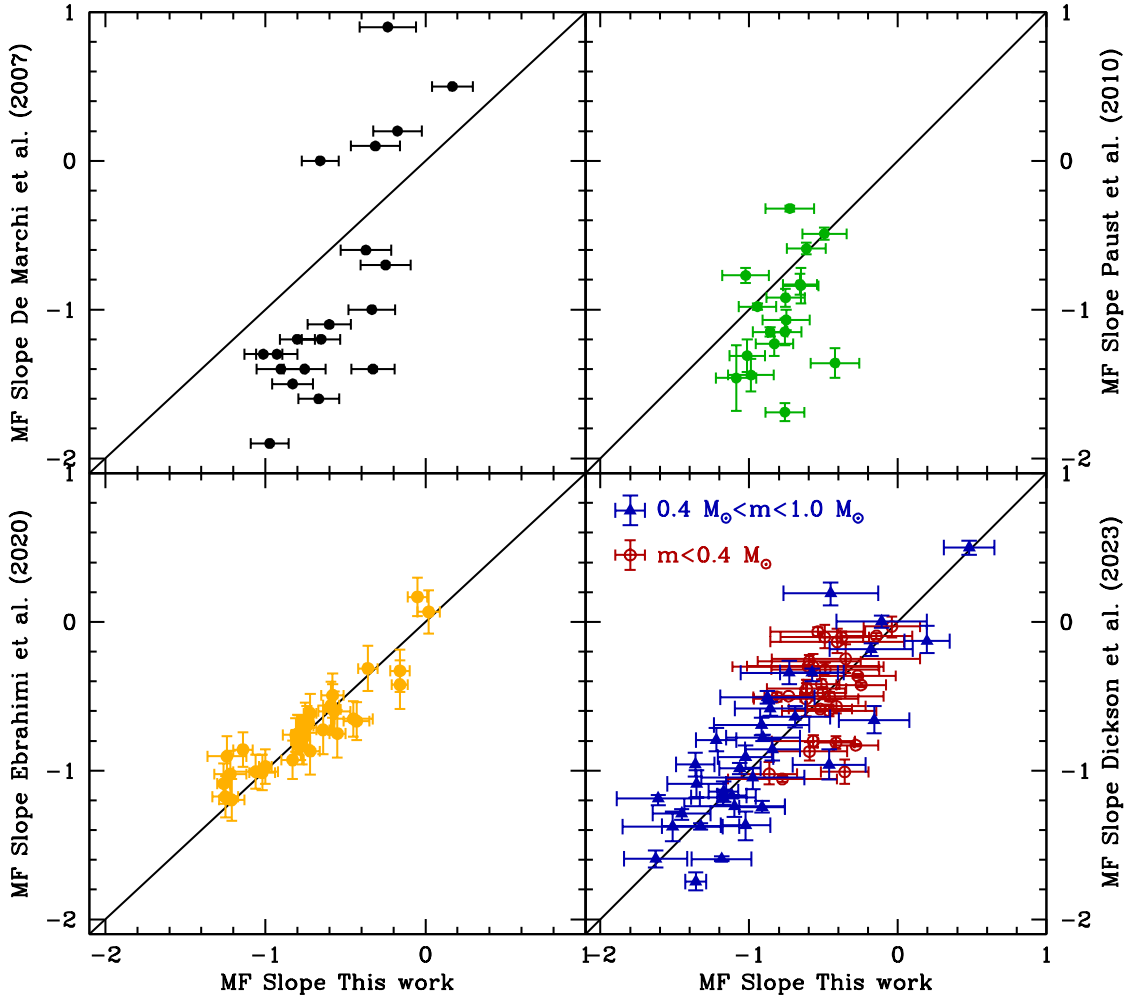


**Figure 6.** Comparison of the mass function slopes derived in this work against those derived by De Marchi, Paresce & Pulone (2007) (top left panel), Paust et al. (2010) (top right panel), Ebrahimi et al. (2020) (bottom left panel) and Dickson et al. (2023) (bottom right panel) for the clusters in common. We use single power-law slopes for the comparison with the literature papers except when comparing with Dickson et al. (2023), where we fit mass functions to stars in the low and intermediate mass regime separately.

obtain excellent agreement with the mass functions derived by Ebrahimi et al. (2020) with almost all clusters being in agreement within the quoted error bars. This is despite the fact that the fitted isochrones as well as the method how the mass functions were derived are different between our paper and Ebrahimi et al. (2020). The bottom right panel finally compares our mass function slopes with the ones from Dickson et al. (2023). Here we compare the mass function slopes separately for stars with masses above and below  $0.4 M_{\odot}$ . The slopes from Dickson et al. (2023) are not completely independent of ours since they also used our HST star counts. However the method to get from the star count data in different HST fields to the global mass function is different to ours. Nevertheless, the agreement between the derived mass function slopes is very good both for stars with  $m > 0.4 M_{\odot}$  and for stars with  $m < 0.4 M_{\odot}$ .

#### 4.4 Globular cluster mass functions

We next discuss the mass function of the full sample of MW globular clusters and LMC/SMC stars clusters, derived by

fitting the grid of  $N$ -body simulations calculated in the previous section against their observed mass function slopes. Fig. 7 shows the global mass function slopes of Galactic globular clusters and LMC/SMC star clusters as a function of the dynamical age (left panel) and the fractional lifetime of the clusters (right panel). We have defined the dynamical age as the ratio of the age of a cluster over its relaxation time and the fractional lifetime as the ratio of the cluster age to the estimated dissolution time. We fit the mass function of each cluster using either only the low mass stars  $m < 0.40 M_{\odot}$  (upper panels), the intermediate-mass stars with  $0.40 M_{\odot} < m < 1.0 M_{\odot}$  (middle panels) or high mass stars with  $m > 1 M_{\odot}$  (lower panels). Since Galactic globular clusters do not contain high-mass main-sequence stars with  $m > 1 M_{\odot}$ , we have results for them only for the upper and middle panels, while for the LMC/SMC clusters we have no results for the  $m < 0.40 M_{\odot}$  stars since these are too faint to be observed due to the large cluster distances.

It can be seen that we obtain a strong correlation between the mass function slopes and either the dynamical age or fractional dissolution time for the low and intermediate mass stars, with Spearman-rank order coefficients equal to

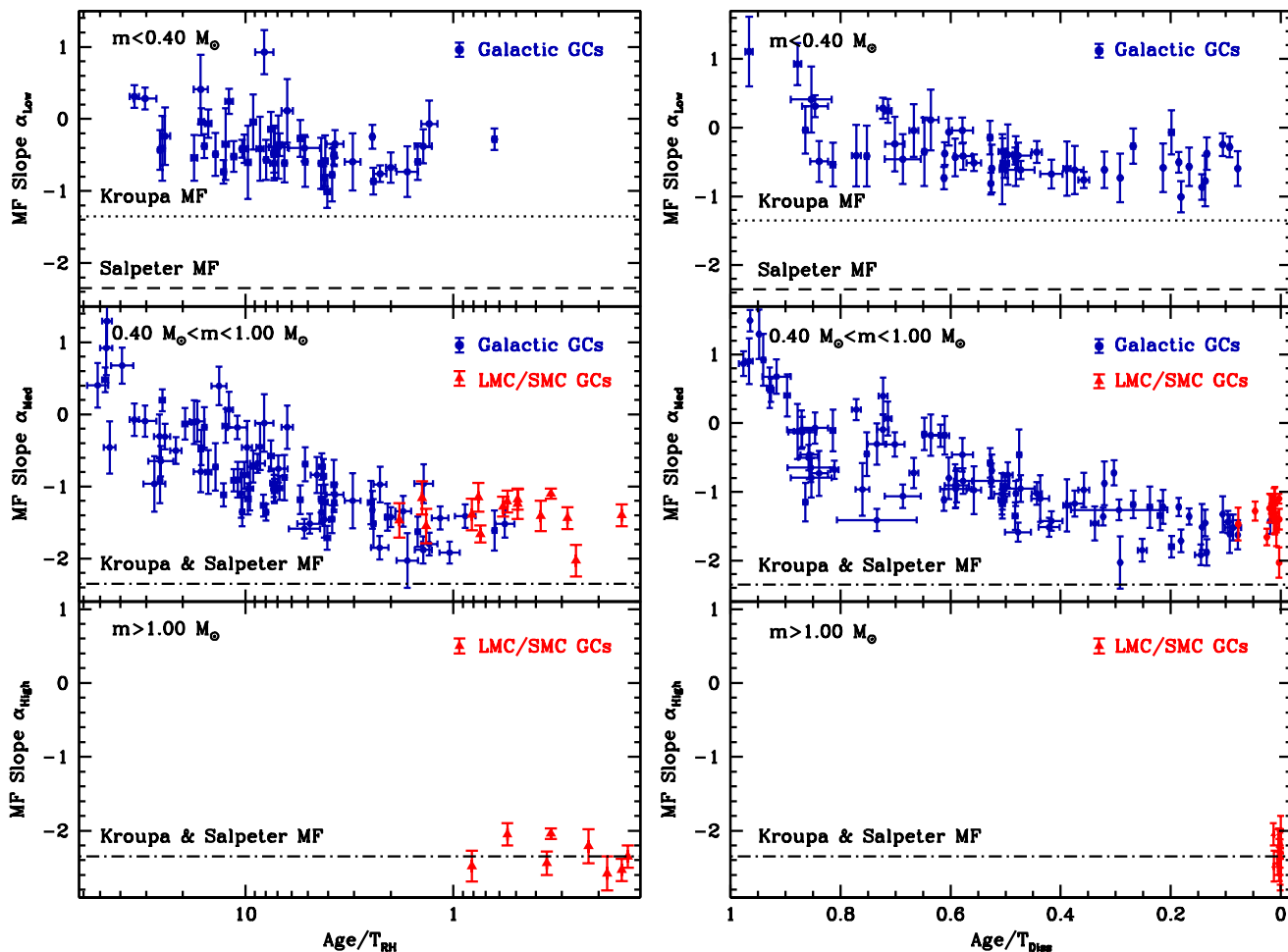


**Figure 7.** Global mass function slopes  $\alpha$  as a function of the dynamical ages of globular clusters (left panel) and the ratio of their ages to their lifetimes (right panel). Globular clusters follow a narrow sequence going from clusters with negative mass function slopes (many low-mass stars) and relaxation times/lifetimes that are larger than their ages to clusters highly depleted in low-mass stars for clusters with short relaxation times/lifetimes. Clusters are also considerably more depleted in low-mass stars than canonical Kroupa/ Salpeter mass functions.

$r = 0.85$  and  $r = 0.81$  respectively. In particular, the mass function slopes for low and intermediate mass stars are more strongly negative for the dynamically least evolved clusters and become gradually less negative for clusters with smaller relaxation times and smaller lifetimes (relative to their ages). As will be discussed further below, the correlation of mass function slopes with dynamical ages and fractional lifetimes is likely due to the internal evolution of the clusters and not a sign of initial variations. If this is the case, the present-day mass functions of clusters on the right hand side in both diagrams should reflect their initial mass functions, justifying the cluster selection made in sec. 4.1. There is also very good agreement between the mass functions of the Galactic globular clusters and the LMC/SMC clusters in the regions of overlap. For the high mass stars we have data only for the LMC/SMC star clusters. Since these clusters are on average more extended than Galactic globular clusters, they have large relaxation times and our data does not allow us to see an evolution of the high-mass star mass function as we can only probe the less evolved and presumably primordial distribution. The same applies to the fractional lifetime distribution, due to the young ages of the clusters and their

long lifetimes times, the  $\text{Age}/T_{Diss}$  ratio is less than 0.1 for all LMC/SMC clusters.

Using only the least evolved clusters with relaxation times and lifetimes larger than a Hubble time, we find average mass function slopes of  $\alpha_{Low} \approx -0.3$  for  $m < 0.4 M_{\odot}$  stars,  $\alpha_{Low} \approx -1.6$  for stars with  $0.4 M_{\odot} < m < 1.0 M_{\odot}$  and  $-2.3$  for stars with  $m > 1.0 M_{\odot}$ . A Kroupa (2001) mass function has a slope of  $\alpha = -2.3$  for stars more massive than  $0.5 M_{\odot}$  and a slope of  $\alpha = -1.3$  for less massive stars, while a Salpeter mass function has a slope of  $\alpha = -2.3$  for all stars (see dashed and dotted lines in Fig. 7). Our results from the expanded cluster sample again argue for a low-mass star function in globular clusters with significantly fewer low-mass stars compared to a Kroupa/Salpeter mass function. Our mass function below  $0.8 M_{\odot}$  is in good agreement with the power-law mass function slope of  $-1.3$  that Leigh et al. (2012) found from comparing the inner mass functions of 27 globular clusters with the results of Monte Carlo simulations. We also confirm earlier results by Cadelano et al. (2020) for the global mass functions of NGC 7078 and NGC 7099 as well as Hénault-Brunet et al. (2020) for the mass function of NGC 104.

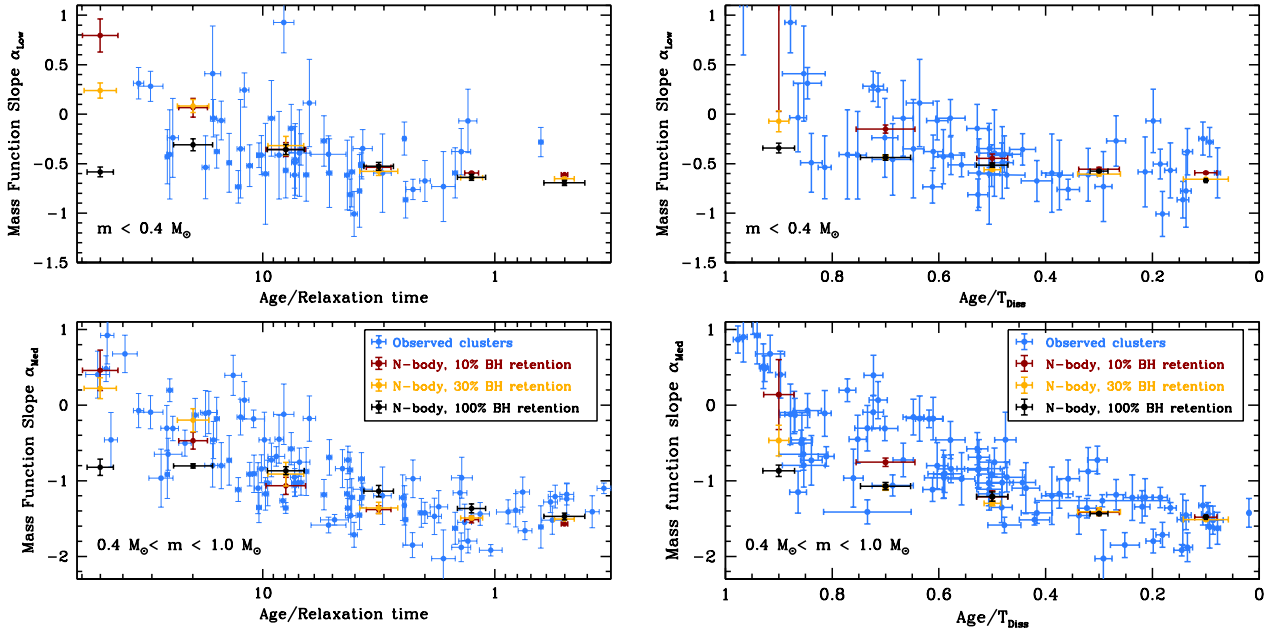


**Figure 8.** Comparison of the derived mass function slopes for Galactic GCs (blue circles) with the results of  $N$ -body simulations of star clusters dissolving in tidal fields with an assumed BH retention fraction (upon formation) of 10% (red), 30% (orange) and 100% (black).  $N$ -body models with 10% BH retention fraction follow the observed trends with dynamical age and fractional lifetime very well. 30% BH retention models reproduce the trend with dynamical age well, but reproduce the trend with fractional lifetime less well. 100% BH retention models can't reproduce these trends since they are not able to produce clusters strongly depleted in low-mass stars.

#### 4.5 Comparison with $N$ -body simulations

We next investigate if the observed correlations of the stellar mass function with dynamical age and fractional lifetime that we find for Milky Way globular clusters can be explained by the dynamical cluster evolution and the constraints the results can put on the black hole retention fraction in star clusters. We again use the  $N$ -body simulations from Table 1 for 10% retention fraction. In order to test the dependence of the results on the assumed black hole retention fraction, we also re-run all simulations in Table 1 with 30% and 100% BH retention fractions. In these new simulations, we keep the neutron star retention fraction at 10%.

Fig. 8 shows the comparison of the mass function slopes of observed globular clusters with the results of the  $N$ -body simulations. It can be seen that models with a 10% retention fraction of black holes reproduce the observed mass function trends with dynamical age and fractional lifetime very closely, showing that the differences in the stellar mass function between different clusters are unlikely to arise due to initial differences, but can be explained by dynamical changes due to mass segregation and the preferential loss of low-mass stars. The models also show that the slope of the low-mass star mass function changes significantly less over the course of evolution compared to the slope of stars in the mass range  $0.4$  to  $1.0 M_{\odot}$ . The reason for this behavior is probably that low mass stars are pushed towards the outer parts where the relaxation time is long and there is little further mass segregation between these stars. Hence they are lost at a similar rate independent of their mass.

Clusters starting with a 100% black hole retention fraction never reach a state where they are highly depleted in

low-mass stars. This is because a large number of stellar-mass black holes in a star cluster prevents mass segregation between the lower mass stars (e.g. Lützgendorf et al. 2013; Weatherford et al. 2018). As a result, clusters with many black holes are unable to reproduce the observed mass function evolution, especially for the dynamically more evolved clusters. Clusters with 30% BH retention rates can reproduce the trend with dynamical age but don't reproduce the trend with dissolution time towards the final stages. We therefore conclude that a high initial BH retention fraction is ruled out by our data. Given our chosen mass function, and assuming a 30% retention fraction of black holes leads to a typical ratio in the number of black holes to the total number of stars of around  $N_{BH}/N_{*} \approx 1.0 \cdot 10^{-3}$  directly after BH formation. This ratio further decreases due to BH binary formation and subsequent hardening and ejections of the black holes from the cluster centres. Assuming a decrease by a factor of two to five in the number of BHs surviving up to a Hubble time, we predict between 30 to 100 (300 to 1000) remaining BHs in a  $10^5 M_{\odot}$  ( $10^6 M_{\odot}$ ) globular cluster. These estimates are in good agreement with estimates for the number of stellar-mass BHs inferred from observations of the surface density profiles (Arca Sedda, Askar & Giersz 2018; Askar, Arca Sedda & Giersz 2018) and the internal amount of mass segregation (Weatherford et al. 2018) of Galactic globular clusters. They are also in agreement with what Dickson et al. (2023) find from a comparison of multi-mass King models with the observed kinematics of globular clusters.

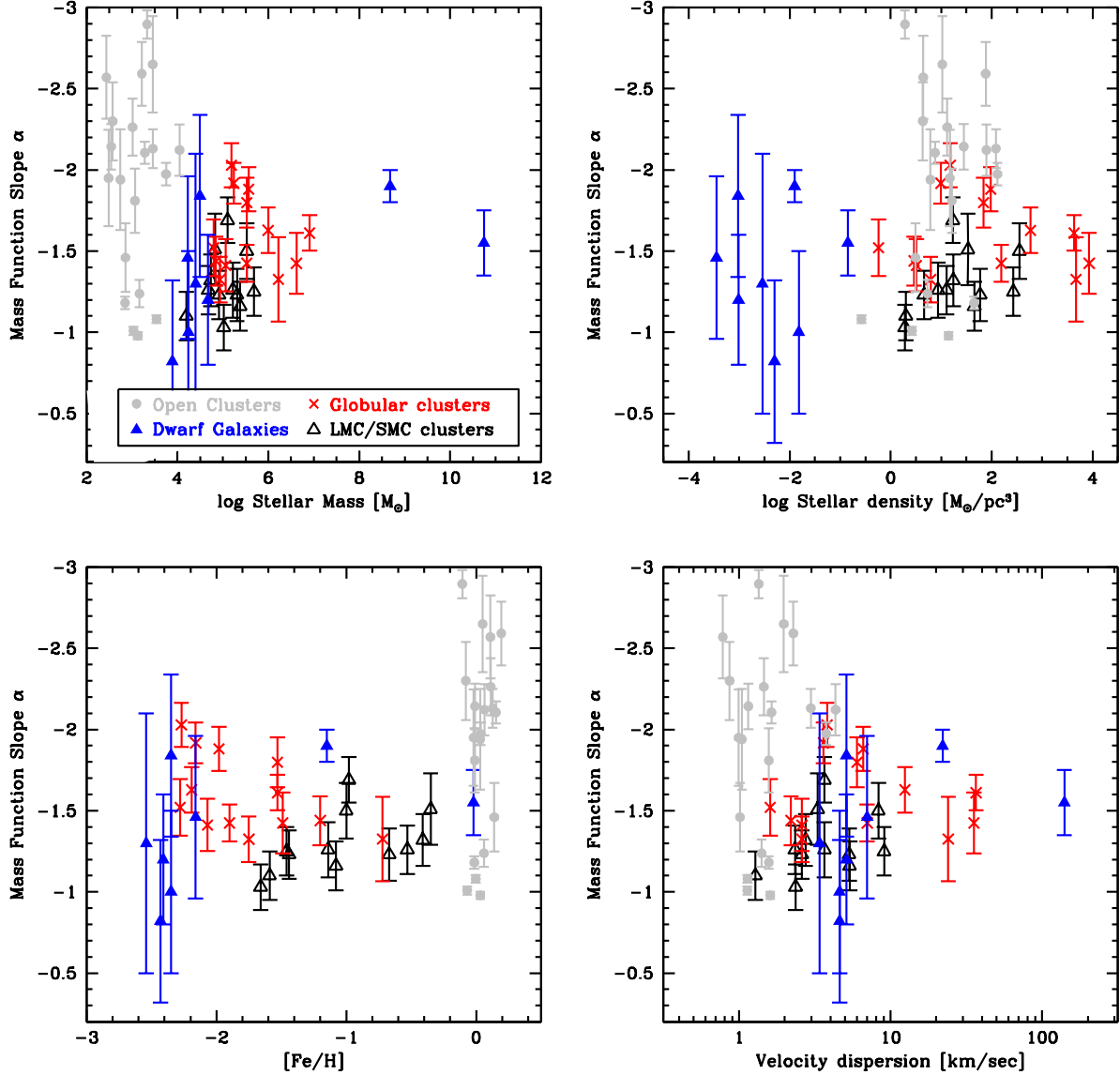


**Figure 9.** Stellar mass function slopes as a function of (clockwise from top left) the mass of the stellar system, its stellar density, velocity dispersion and metallicity. Star clusters studied in this paper are shown by red crosses and black, open triangles. We only show clusters with relaxation times and lifetimes larger than their ages for which the present-day mass function should still be close to the initial one. In addition we also show stellar mass functions for Milky Way open clusters from Ebrahimi, Sollima & Haghi (2022) and Cordini et al. (2023) (grey circles) as well as those for field stars in several nearby dwarf galaxies (blue filled triangles). There does not seem to be a correlation of the mass function slope with any of the depicted parameters or stellar systems. The only exception seem to be open cluster mass functions, which are on average more bottom-heavy.

#### 4.6 Environmental dependency of the stellar mass function

In order to explore the influence of the external environment on the stellar mass function, we depict in Fig. 9 the mass-function slopes that we have derived as a function of different cluster parameters. Shown are (clockwise from top-left), the cluster mass, the average density inside the half-mass radius of the cluster and the central velocity dispersion of the cluster and the cluster metallicity. We restrict our fits to intermediate-mass stars in the range  $0.4 M_{\odot} < m < 1.0 M_{\odot}$  since this is the mass function range for which we have the most data and the only one where LMC/SMC clusters

and globular clusters overlap. We depict only clusters with remaining lifetimes several times larger than their ages since for these the present-day mass functions should still be close to the initial ones. In order to correct for mass loss due to stellar evolution, we increase the present-day cluster masses by a factor of two to get the initial masses. We also assume that stellar evolution induced mass loss leads to an adiabatic expansion of the cluster so that the initial half-mass radius was half the present-day value. Both assumptions lead to a factor 16 increase of the initial density over the present-day one and a factor two increase of the initial velocity dispersion. The true increase could be higher if the dynamical cluster evolution has led to an expansion of a cluster, how-

ever given the large relaxation times of the depicted clusters, this is likely not a large effect.

We extend our sample beyond star clusters by adding the mass function determinations from Geha et al. (2013) and Gennaro et al. (2018) for six ultra-faint dwarf galaxies and from Kalirai et al. (2013) for field stars in the SMC. We also add data about the IMF of Milky Way disc stars in the solar neighborhood derived by Sollima (2019) based on Gaia DR2 parallaxes and magnitudes. These eight measurements form the galaxy sample in Fig. 9. We take the metallicities, masses, sizes and velocity dispersions of the dwarf galaxies from Simon (2019). The galaxy data covers the sub-solar mass function, making it directly comparable to the data from the cluster sample. We finally add mass function determinations for open clusters in the solar neighborhood recently derived by Ebrahimi, Sollima & Haghi (2022) and Cordoni et al. (2023) based on Gaia DR3 data. We use only clusters with relaxation times larger than their ages from both papers in order to minimise the influence of dynamical evolution and use the mass function slopes for stars with  $m < 1 M_{\odot}$  to make the open cluster data comparable to the data of the other systems.

As can be seen, most mass functions are compatible with a slope of about  $\alpha \approx -1.5$ , without any obvious dependency of the stellar mass function slope on either the mass, the density, the metallicity or the internal velocity dispersion of the stellar system. The visual impression is confirmed by Spearman rank order tests which do not indicate a significant correlation between any of the depicted parameters and the mass function slope. Marks & Kroupa (2010) suggested a systematic change of the initial stellar mass function with the density of the star forming cloud that forms a globular cluster. However, given our data, at least the sub-solar IMF seems more or less independent on density over nearly eight orders of magnitude. We furthermore see no evidence for a metallicity dependency of the stellar IMF for globular clusters as has been argued by Zonoozi, Haghi & Kroupa (2016). In addition, as discussed in sec. 4.4, stars with masses more massive than  $1.0 M_{\odot}$  seem to follow a Salpeter mass function for all studied LMC/SMC clusters, similar to the mass function seen for massive stars in a wide range of environments (Bastian, Covey & Meyer 2010), again arguing against a variation of the high-mass IMF with metallicity. The last conclusion is confirmed by Dickson et al. (2023), who find that the kinematic data of globular clusters, when accounting for stars which have evolved into remnants at the present-day, is fully compatible with a Salpeter IMF above  $1 M_{\odot}$ . Dickson et al. (2023) also find no correlation between this mass function and cluster metallicity.

The only exception could be open clusters in the solar neighborhood, shown by grey circles in Fig. 9, for which we find an average mass function slope of  $\alpha = -1.9$ . This is about 0.4 dex steeper than the average slopes that we find for the other systems and could indicate a change in the IMF happening at either solar metallicity, low masses, young ages, or a combination of these parameters. The open cluster data however also shows a large scatter in the slopes for individual clusters, which range from about -1 to -3, and which seems to be much larger than what can be explained by errors in the data alone. Hence it is possible that there could still be some systematic error in the open cluster data, or that the open cluster mass functions are already influ-

enced by dynamical effects. Detailed  $N$ -body modeling of the depicted clusters and their dynamical evolution in the Milky Way might therefore be necessary to test if the open clusters formed with their present-day mass functions.

## 5 CONCLUSIONS

We have determined the stellar mass functions of 91 Milky Way globular clusters and 29 massive star clusters in the Large and Small Magellanic Clouds by fitting  $N$ -body models to star count data derived from over 300 individual HST fields. We find that the stellar mass functions of dynamically unevolved star clusters, characterized by relaxation times  $T_{RH}$  of the order of their ages and/or lifetimes  $T_{Diss}$  significantly larger than their ages, are well described by a multi-stage power-law mass function  $N(m) \sim m^{\alpha}$  with break masses at  $0.4 M_{\odot}$  and  $1 M_{\odot}$  and power law-slopes of  $\alpha_{Low} = -0.3 \pm 0.2$ ,  $\alpha_{Med} = -1.65 \pm 0.20$  and  $\alpha_{High} = -2.30 \pm 0.20$  for the low-mass, intermediate-mass and high-mass stars respectively. An alternative description of the mass functions of these clusters is a log-normal mass function with characteristic mass  $\log M_C = -0.36$  and width  $\sigma_C = 0.28$  that transitions into a power-law mass function at  $1 M_{\odot}$ . The mass function we find has fewer low-mass stars compared to the mass functions suggested by Kroupa (2001) or Chabrier (2003), which are measured in the solar neighborhood and are significantly more bottom heavy. Our results therefore add to the increasing evidence that the stellar mass function varies across different environments.

We also find that star clusters with relaxation times or lifetimes much less than their ages are depleted in low-mass stars. The amount of depletion is in agreement with  $N$ -body simulations that model the effects of mass segregation and preferential depletion of low-mass stars due to the external tidal fields on star clusters. Most investigated star clusters are therefore compatible with having formed with the same stellar mass function. By comparing the location of clusters in the dynamical age and age over lifetime vs. mass function slope planes with the results of direct  $N$ -body simulations, we also find that the mass function changes are best reproduced if most black holes that form in star clusters receive strong natal kicks at birth that remove them from their parent clusters. The reason for this is that clusters which retain most of their black holes do not become sufficiently depleted in low-mass stars to explain the observations. We predict a remaining black hole population in star clusters of no more than a few hundred black holes for clusters with masses up to  $10^6 M_{\odot}$ . This estimate agrees with what has been found earlier from an analysis of the surface density profiles of globular clusters (Askar, Arca Sedda & Giersz 2018) and their amount of mass segregation (Weatherford et al. 2018).

Our data finally argues against IMF variations with either the metallicity, mass, density or velocity dispersion of star clusters, at least among relatively old stars and for metallicities below the solar one. (Chon, Omukai & Schneider 2021) argued, based on hydrodynamical simulations of star formation, for a shift towards more bottom-heavy mass functions in higher metallicity environments. If real this shift must happen at metallicities  $[Fe/H] < -2.3$  which is not probed by our data.

A mass function described by our findings leads to an

average stellar mass at birth of  $\langle m \rangle = 1.0 M_{\odot}$  and an about twice larger fraction of massive stars with  $m_* > 10 M_{\odot}$  that evolve into black holes and neutron stars per unit stellar mass compared to a Kroupa (2001) mass function. Furthermore, at birth such a mass function has a nearly twice as large fraction of mass in  $m > 10 M_{\odot}$  stars compared to  $m < 0.8 M_{\odot}$  stars than a Kroupa (2001) mass function. Our results therefore argue for more self-enrichment of stars in globular clusters and, if they can be generalized to field stars, overall more chemical enrichment in low metallicity environments. Due to the larger mass fraction in high-mass stars which can pollute lower mass stars forming in the same cluster, our mass function would also help alleviate the so-called mass budget problem in globular clusters (D’Antona & Caloi 2008), according to which the observed number of chemically enriched, second population stars is far higher than expected based on standard pollution scenarios. A factor two increase in the mass ratio of massive to low-mass stars is however not enough to explain the observed number of second population stars since proposed scenarios for the origin of second generation stars fail by at least a factor of 10 to explain the current number ratios (Decressin, Charbonnel & Meynet 2007; Conroy 2012). Furthermore, these calculations assume that all of the the ejecta of massive stars are being used to enrich low-mass stars, which seems an optimistic assumption given that some of this material might escape or enrich intermediate-mass stars.

A mass function described by our findings also increases the amount of gravitational waves created by inspiraling black holes and neutron stars compared to a standard mass function (Weatherford et al. 2021). However the number of inspiraling black holes also depends strongly on the binary and higher order multiple properties of massive stars (e.g. Belczynski et al. 2016; Antonini, Toonen & Hamers 2017) and we currently do not have good constraints on these. An independent test of our results can be obtained from stellar kinematics since the large number of compact remnants predicted by the mass function found here should lead to an increase of stellar velocities over that predicted by standard mass functions with fewer remnants. We will investigate this point for a number of well observed globular clusters in a companion paper (Dickson et al. 2023).

## ACKNOWLEDGMENTS

We dedicate this paper to the memory of our friend and long-term collaborator Antonio Sollima who passed away prior to the publication of this paper. Antonio was a kind and humble scientist who made several key contributions to star cluster research, and he will be greatly missed. We thank Emanuele Dalessandro, Hamid Ebrahimi, Mojjyaba Taheri, Andrés del Pino, Sven Martens and Giacomo Cordoni for sharing their kinematic and mass function data with us. We also thank an anonymous referee for comments that improved the presentation of the paper. VHB acknowledges the support of the Natural Sciences and Engineering Research Council of Canada (NSERC) through grant RGPIN-2020-05990. ND is grateful for the support of the Durland Scholarship in Graduate Research. This work is based on observations made with the NASA/ESA Hubble Space Telescope, obtained from the data archive at

the Space Telescope Science Institute. STScI is operated by the Association of Universities for Research in Astronomy, Inc. under NASA contract NAS 5-26555. Part of this work was performed on the OzSTAR national facility at Swinburne University of Technology. The OzSTAR program receives funding in part from the Astronomy National Collaborative Research Infrastructure Strategy (NCRIS) allocation provided by the Australian Government.

## DATA AVAILABILITY

Data is available upon request.

## REFERENCES

- Abdurro’uf et al., 2022, *ApJS*, 259, 35  
Abe M., Yajima H., Khochfar S., Dalla Vecchia C., Omukai K., 2021, *MNRAS*, 508, 3226  
Abel T., Bryan G. L., Norman M. L., 2002, *Science*, 295, 93  
Antonini F., Toonen S., Hamers A. S., 2017, *ApJ*, 841, 77  
Aoyama S., Ouchi M., Harikane Y., 2021, arXiv e-prints, arXiv:2111.02624  
Arca Sedda M., Askar A., Giersz M., 2018, *MNRAS*, 479, 4652  
Askar A., Arca Sedda M., Giersz M., 2018, *MNRAS*, 478, 1844  
Barth N. A., Gerber J. M., Boberg O. M., Friel E. D., Vesperini E., 2020, *MNRAS*, 494, 4548  
Bastian N., Covey K. R., Meyer M. R., 2010, *ARA&A*, 48, 339  
Baumgardt H., 2017, *MNRAS*, 464, 2174  
Baumgardt H., Faller J., Meinhold N., McGovern-Greco C., Hilker M., 2022, *MNRAS*, 510, 3531  
Baumgardt H., Hilker M., 2018, *MNRAS*, 478, 1520  
Baumgardt H., Hilker M., Sollima A., Bellini A., 2019, *MNRAS*, 482, 5138  
Baumgardt H., Makino J., 2003, *MNRAS*, 340, 227  
Baumgardt H., Parmentier G., Anders P., Grebel E. K., 2013, *MNRAS*, 430, 676  
Baumgardt H., Sollima A., Hilker M., 2020, *PASA*, 37, e046  
Baumgardt H., Vasiliev E., 2021, *MNRAS*, 505, 5957  
Belczynski K., Repetto S., Holz D. E., O’Shaughnessy R., Bulik T., Berti E., Fryer C., Dominik M., 2016, *ApJ*, 819, 108  
Bennet P., Alfaro-Cuello M., Pino A. d., Watkins L. L., van der Marel R. P., Sohn S. T., 2022, *ApJ*, 935, 149  
Bressan A., Marigo P., Girardi L., Salasnich B., Dal Cero C., Rubele S., Nanni A., 2012, *MNRAS*, 427, 127  
Bromm V., Coppi P. S., Larson R. B., 2002, *ApJ*, 564, 23  
Bromm V., Yoshida N., Hernquist L., McKee C. F., 2009, *Nature*, 459, 49  
Buder S. et al., 2021, *MNRAS*, 506, 150  
Cadelano M., Dalessandro E., Webb J. J., Vesperini E., Lattanzio D., Beccari G., Gomez M., Monaco L., 2020, *MNRAS*, 499, 2390  
Calura F., Menci N., 2009, *MNRAS*, 400, 1347  
Cappellari M. et al., 2012, *Nature*, 484, 485  
Cardelli J. A., Clayton G. C., Mathis J. S., 1989, *ApJ*, 345, 245

- Carretta E., Bragaglia A., Gratton R., D’Orazi V., Lucatello S., 2009, *A&A*, 508, 695
- Chabrier G., 2003, *PASP*, 115, 763
- Chen Y., Bressan A., Girardi L., Marigo P., Kong X., Lanza A., 2015, *MNRAS*, 452, 1068
- Chen Y., Girardi L., Bressan A., Marigo P., Barbieri M., Kong X., 2014, *MNRAS*, 444, 2525
- Chon S., Omukai K., Schneider R., 2021, *MNRAS*, 508, 4175
- Clauset A., Shalizi C. R., Newman M. E. J., 2009, *SIAM Review*, 51, 661
- Cohen R. E., Bellini A., Libralato M., Correnti M., Brown T. M., Kalirai J. S., 2021, *AJ*, 161, 41
- Conroy C., 2012, *ApJ*, 758, 21
- Cordoni G. et al., 2023, arXiv e-prints, arXiv:2302.03685
- Crestani J., Alves-Brito A., Bono G., Puls A. A., Alonso-García J., 2019, *MNRAS*, 487, 5463
- Cui X.-Q. et al., 2012, *Research in Astronomy and Astrophysics*, 12, 1197
- Dalessandro E., Raso S., Kamann S., Bellazzini M., Vesperini E., Bellini A., Beccari G., 2021, *MNRAS*, 506, 813
- Dalgleish H. et al., 2020, *MNRAS*, 492, 3859
- D’Antona F., Caloi V., 2008, *MNRAS*, 390, 693
- De Angeli F., Piotto G., Cassisi S., Busso G., Recio-Blanco A., Salaris M., Aparicio A., Rosenberg A., 2005, *AJ*, 130, 116
- De Marchi G., Paresce F., Pulone L., 2007, *ApJ*, 656, L65
- Decressin T., Charbonnel C., Meynet G., 2007, *A&A*, 475, 859
- del Pino A. et al., 2022, *ApJ*, 933, 76
- Dickson N., Hénault-Brunet V., Baumgardt H., Gieles M., Smith P. J., 2023, *MNRAS*, submitted
- Dolphin A., 2016, *DOLPHOT: Stellar photometry*
- Dolphin A. E., 2000, *PASP*, 112, 1383
- Dotter A., Chaboyer B., Jevremović D., Kostov V., Baron E., Ferguson J. W., 2008, *ApJS*, 178, 89
- Dotter A. et al., 2010, *ApJ*, 708, 698
- Ebrahimi H., Sollima A., Haghi H., 2022, *MNRAS*, 516, 5637
- Ebrahimi H., Sollima A., Haghi H., Baumgardt H., Hilker M., 2020, *MNRAS*, 494, 4226
- Ferraro F. R. et al., 2018, *ApJ*, submitted
- Gaia Collaboration et al., 2022, arXiv e-prints, arXiv:2208.00211
- Geha M. et al., 2013, *ApJ*, 771, 29
- Gennaro M. et al., 2018, *ApJ*, 855, 20
- Giesers B. et al., 2019, *A&A*, 632, A3
- Göttgens F. et al., 2021, *MNRAS*, 507, 4788
- Gunn J. E., Griffin R. F., 1979, *AJ*, 84, 752
- Harris W. E., 1996, *AJ*, 112, 1487 (2010 edition)
- Hénault-Brunet V., Gieles M., Strader J., Peuten M., Balbinot E., Douglas K. E. K., 2020, *MNRAS*, 491, 113
- Johnson C. I., Caldwell N., Michael Rich R., Mateo M., Bailey J. I., 2019, *MNRAS*, 485, 4311
- Johnson C. I., Dupree A. K., Mateo M., Bailey, John I. I., Olszewski E. W., Walker M. G., 2020, *AJ*, 159, 254
- Kacharov N. et al., 2022, *ApJ*, 939, 118
- Kalirai J. S. et al., 2013, *ApJ*, 763, 110
- Kamann S. et al., 2018, *MNRAS*, 473, 5591
- Katz D. et al., 2022, arXiv e-prints, arXiv:2206.05902
- Khalaj P., Baumgardt H., 2013, *MNRAS*, 434, 3236
- King I., 1962, *AJ*, 67, 471
- King I. R., 1966, *AJ*, 71, 64
- Kirby E. N., Duggan G., Ramirez-Ruiz E., Macias P., 2020, *ApJ*, 891, L13
- Koch A., Xu S., Rich R. M., 2019, *A&A*, 627, A70
- Kroupa P., 2001, *MNRAS*, 322, 231
- Krumholz M. R., 2014, *Phys. Rep.*, 539, 49
- Krumholz M. R., Cunningham A. J., Klein R. I., McKee C. F., 2010, *ApJ*, 713, 1120
- Leigh N., Umbreit S., Sills A., Knigge C., de Marchi G., Glebbeek E., Sarajedini A., 2012, *MNRAS*, 422, 1592
- Libralato M. et al., 2022, *ApJ*, 934, 150
- Lützgendorf N. et al., 2013, *A&A*, 552, A49
- Marín-Franch A. et al., 2009, *ApJ*, 694, 1498
- Marino A. F. et al., 2021, *ApJ*, 923, 22
- Marks M., Kroupa P., 2010, *MNRAS*, 406, 2000
- Martens S. et al., 2023, arXiv e-prints, arXiv:2301.08675
- Milone A. P. et al., 2023, *MNRAS*, submitted
- Muñoz C., Geisler D., Villanova S., Sarajedini A., Freligg H., Vargas C., Monaco L., O’Connell J., 2021, *MNRAS*, 506, 4676
- Nitadori K., Aarseth S. J., 2012, *MNRAS*, 424, 545
- Nony T. et al., 2023, arXiv e-prints, arXiv:2301.07238
- Paust N. E. Q. et al., 2010, *AJ*, 139, 476
- Pouteau Y. et al., 2022, *A&A*, 664, A26
- Rain M. J., Villanova S., Munõz C., Valenzuela-Calderon C., 2019, *MNRAS*, 483, 1674
- Salpeter E. E., 1955, *ApJ*, 121, 161
- Simon J. D., 2019, *ARA&A*, 57, 375
- Sollima A., 2019, *MNRAS*, 489, 2377
- Sollima A., Dalessandro E., Beccari G., Pallanca C., 2017, *MNRAS*, 464, 3871
- Taheri M. et al., 2022, *AJ*, 163, 187
- Valcin D., Bernal J. L., Jimenez R., Verde L., Wandelt B. D., 2020, *Journal of Cosmology and Astroparticle Physics*, 2020, 002
- van Dokkum P. G., Conroy C., 2010, *Nature*, 468, 940
- VandenBerg D. A., Brogaard K., Leaman R., Casagrande L., 2013, *ApJ*, 775, 134
- Vasiliev E., Baumgardt H., 2021, *MNRAS*, 505, 5978
- Černiauskas A., Kučinskas A., Klevas J., Bonifacio P., Ludwig H. G., Caffau E., Steffen M., 2018, *A&A*, 616, A142
- Vesperini E., Heggie D. C., 1997, *MNRAS*, 289, 898
- Wan Z. et al., 2021, *MNRAS*, 502, 4513
- Wan Z. et al., 2023, *MNRAS*, in preparation
- Weatherford N. C., Chatterjee S., Rodriguez C. L., Rasio F. A., 2018, *ApJ*, 864, 13
- Weatherford N. C., Fragione G., Kremer K., Chatterjee S., Ye C. S., Rodriguez C. L., Rasio F. A., 2021, *ApJ*, 907, L25
- Webb J. J., Leigh N. W. C., 2015, *MNRAS*, 453, 3278
- Zonoozi A. H., Haghi H., Kroupa P., 2016, *ApJ*, 826, 89

## APPENDIX A: FINDING CHARTS OF THE HST FIELDS

The HST finding charts are available as supplementary material in the electronic version.

**Table B1.** The adopted ages and metallicities, the best-fitting distance moduli and reddening values, the lower and upper mass limits of the mass function fits, and the derived mass function slopes for the globular clusters studied in this paper. The final three columns give  $\alpha_{Tot}$ , the best-fitting single power-law slope fit over the whole mass range, as well as the mass function slopes  $\alpha_{Low}$  and  $\alpha_{Med}$  for stars with masses below and above  $0.40 M_{\odot}$ .

Cluster	Age [Gyr]	[Fe/H]	Dist. mod.	E(B-V)	$m_{Low}$ [ $M_{\odot}$ ]	$m_{High}$ [ $M_{\odot}$ ]	$\alpha_{Tot}$	$\alpha_{Low}$	$\alpha_{Med}$
Arp 2	12.4	-1.74	17.29	0.14	0.41	0.80	$-0.75 \pm 0.14$	—	$-0.75 \pm 0.14$
E 3	12.1	-0.73	14.18	0.37	0.35	0.85	$+0.88 \pm 0.24$	—	$+0.40 \pm 0.31$
IC 4499	12.1	-1.62	16.38	0.26	0.28	0.81	$-1.23 \pm 0.15$	$-0.07 \pm 0.32$	$-1.80 \pm 0.16$
Lynga 7	13.2	-1.01	14.39	0.80	0.32	0.80	$+0.30 \pm 0.16$	—	$+0.39 \pm 0.27$
NGC 104	12.4	-0.76	13.29	0.05	0.22	0.86	$-0.65 \pm 0.12$	$-0.25 \pm 0.17$	$-1.33 \pm 0.26$
NGC 288	11.7	-1.32	14.83	0.04	0.22	0.82	$-0.66 \pm 0.12$	$-0.51 \pm 0.12$	$-0.98 \pm 0.35$
NGC 362	11.0	-1.30	14.80	0.03	0.26	0.82	$-0.76 \pm 0.13$	—	$-0.91 \pm 0.25$
NGC 1261	11.0	-1.27	16.07	0.02	0.33	0.83	$-0.61 \pm 0.13$	$-0.36 \pm 0.16$	$-1.02 \pm 0.17$
NGC 1851	11.3	-1.18	15.39	0.04	0.20	0.83	$-0.70 \pm 0.13$	$-0.52 \pm 0.21$	$-0.91 \pm 0.15$
NGC 2298	13.1	-1.96	14.96	0.23	0.25	0.77	$+0.17 \pm 0.13$	$+0.31 \pm 0.16$	$-0.07 \pm 0.22$
NGC 2808	11.2	-1.14	15.07	0.21	0.22	0.83	$-0.60 \pm 0.14$	$-0.27 \pm 0.26$	$-1.19 \pm 0.20$
NGC 3201	11.2	-1.51	13.38	0.29	0.24	0.80	$-1.02 \pm 0.16$	$-0.86 \pm 0.19$	$-1.51 \pm 0.34$
NGC 4147	12.5	-1.78	16.39	0.02	0.20	0.77	$-0.05 \pm 0.13$	$+0.28 \pm 0.15$	$-0.09 \pm 0.22$
NGC 4372	13.0	-2.19	13.43	0.53	0.16	0.77	$-0.86 \pm 0.18$	$-0.59 \pm 0.40$	$-1.20 \pm 0.38$
NGC 4590	12.2	-2.27	15.09	0.07	0.18	0.77	$-1.18 \pm 0.14$	$-1.01 \pm 0.23$	$-1.72 \pm 0.17$
NGC 4833	12.9	-1.89	14.11	0.36	0.24	0.77	$-0.34 \pm 0.15$	$-0.04 \pm 0.38$	$-0.73 \pm 0.22$
NGC 5024	12.7	-2.06	16.37	0.03	0.26	0.78	$-1.20 \pm 0.12$	$-0.59 \pm 0.25$	$-1.63 \pm 0.21$
NGC 5053	12.8	-2.30	16.27	0.01	0.23	0.78	$-1.09 \pm 0.14$	$-0.73 \pm 0.35$	$-2.03 \pm 0.38$
NGC 5139	13.2	-1.64	13.67	0.13	0.17	0.80	$-0.80 \pm 0.11$	$-0.28 \pm 0.15$	$-1.61 \pm 0.28$
NGC 5272	12.1	-1.50	15.04	0.01	0.17	0.77	$-1.01 \pm 0.12$	$-0.78 \pm 0.37$	$-1.45 \pm 0.19$
NGC 5286	12.8	-1.70	15.23	0.24	0.37	0.75	$-0.73 \pm 0.16$	—	$-0.93 \pm 0.20$
NGC 5466	12.6	-2.31	16.07	0.03	0.21	0.78	$-0.86 \pm 0.12$	$-0.76 \pm 0.14$	$-0.97 \pm 0.25$
NGC 5897	12.3	-1.90	15.49	0.14	0.24	0.79	$-1.01 \pm 0.11$	$-0.68 \pm 0.21$	$-1.43 \pm 0.14$
NGC 5904	11.7	-1.33	14.37	0.05	0.16	0.79	$-0.76 \pm 0.11$	$-0.50 \pm 0.15$	$-1.22 \pm 0.14$
NGC 5927	11.6	-0.29	14.49	0.43	0.50	0.81	$-0.99 \pm 0.15$	—	$-0.99 \pm 0.15$
NGC 5946	12.0	-1.29	15.13	0.60	0.52	0.80	$-0.64 \pm 0.16$	—	$-0.64 \pm 0.16$
NGC 5986	12.5	-1.63	15.11	0.31	0.43	0.76	$-0.59 \pm 0.17$	$-0.46 \pm 0.36$	$-1.06 \pm 0.20$
NGC 6093	13.0	-1.75	15.13	0.21	0.23	0.76	$-0.45 \pm 0.16$	$-0.04 \pm 0.19$	$-0.46 \pm 0.24$
NGC 6101	12.6	-1.98	15.83	0.13	0.24	0.79	$-0.90 \pm 0.14$	$-0.38 \pm 0.23$	$-1.88 \pm 0.19$
NGC 6121	12.0	-1.18	11.34	0.51	0.14	0.80	$-0.34 \pm 0.15$	$-0.49 \pm 0.30$	$-0.73 \pm 0.33$
NGC 6144	13.2	-1.82	14.51	0.41	0.36	0.76	$+0.07 \pm 0.14$	$+0.24 \pm 0.17$	$+0.07 \pm 0.25$
NGC 6171	13.4	-1.03	13.70	0.43	0.23	0.78	$-0.29 \pm 0.14$	$-0.54 \pm 0.32$	$-0.11 \pm 0.30$
NGC 6205	12.6	-1.58	14.45	0.01	0.30	0.74	$-0.94 \pm 0.12$	—	$-1.36 \pm 0.15$
NGC 6218	13.3	-1.33	13.54	0.21	0.20	0.78	$-0.31 \pm 0.15$	$-0.38 \pm 0.17$	$-0.18 \pm 0.28$
NGC 6254	12.1	-1.57	13.63	0.29	0.22	0.78	$-0.60 \pm 0.13$	$-0.49 \pm 0.36$	$-1.02 \pm 0.18$
NGC 6266	12.3	-1.18	14.03	0.49	0.53	0.81	$-1.14 \pm 0.19$	—	$-1.14 \pm 0.19$
NGC 6273	12.4	-1.76	14.61	0.44	0.43	0.76	$-1.33 \pm 0.20$	—	$-1.33 \pm 0.20$
NGC 6284	11.8	-1.31	15.76	0.33	0.43	0.82	$-0.05 \pm 0.16$	—	$-0.05 \pm 0.16$
NGC 6287	13.9	-2.12	14.50	0.72	0.36	0.76	$-0.57 \pm 0.16$	—	$-0.96 \pm 0.38$
NGC 6293	12.8	-2.01	14.82	0.40	0.24	0.78	$-0.50 \pm 0.20$	$+0.41 \pm 0.48$	$-0.80 \pm 0.29$
NGC 6304	12.0	-0.37	13.94	0.52	0.43	0.89	$-0.40 \pm 0.14$	—	$-0.40 \pm 0.14$
NGC 6333	12.6	-1.79	14.60	0.38	0.36	0.78	$-0.39 \pm 0.21$	—	$-0.46 \pm 0.36$
NGC 6341	13.0	-2.35	14.65	0.02	0.15	0.77	$-0.83 \pm 0.12$	$-0.41 \pm 0.12$	$-1.35 \pm 0.20$
NGC 6342	12.5	-0.49	14.52	0.53	0.41	0.82	$+0.65 \pm 0.17$	—	$+0.65 \pm 0.17$
NGC 6352	11.8	-0.62	13.67	0.30	0.23	0.83	$-0.37 \pm 0.16$	$-0.35 \pm 0.50$	$-0.16 \pm 0.24$
NGC 6355	13.2	-1.33	14.69	0.87	0.50	0.78	$-0.50 \pm 0.19$	—	$-0.50 \pm 0.19$
NGC 6362	12.7	-1.07	14.42	0.08	0.21	0.80	$-0.49 \pm 0.15$	$-0.59 \pm 0.35$	$-0.69 \pm 0.23$
NGC 6366	11.7	-0.59	12.68	0.76	0.39	0.83	$-0.32 \pm 0.17$	$-0.41 \pm 0.44$	$-0.45 \pm 0.32$
NGC 6388	10.9	-0.45	15.34	0.34	0.40	0.84	$-1.01 \pm 0.18$	—	$-1.01 \pm 0.18$
NGC 6397	13.3	-1.99	11.97	0.24	0.34	0.78	$-0.32 \pm 0.14$	$-0.43 \pm 0.27$	$-0.92 \pm 0.32$
NGC 6401	13.2	-1.01	14.13	0.96	0.40	0.81	$-0.37 \pm 0.17$	—	$-0.37 \pm 0.17$
NGC 6402	12.0	-1.28	14.80	0.60	0.38	0.81	$-0.81 \pm 0.15$	—	$-0.84 \pm 0.20$
NGC 6426	13.1	-2.36	16.58	0.43	0.24	0.78	$-1.07 \pm 0.14$	$-0.41 \pm 0.18$	$-1.59 \pm 0.15$
NGC 6496	11.4	-0.44	14.91	0.16	0.31	0.82	$-0.25 \pm 0.16$	$+0.11 \pm 0.44$	$-0.18 \pm 0.30$
NGC 6535	12.6	-1.79	14.12	0.48	0.29	0.79	$+1.13 \pm 0.18$	—	$+0.92 \pm 0.38$

**Table B1** – *continued*

Cluster	Age [Gyr]	[Fe/H]	Dist. mod.	E(B-V)	$m_{Low}$ [ $M_{\odot}$ ]	$m_{High}$ [ $M_{\odot}$ ]	$\alpha_{Tot}$	$\alpha_{Low}$	$\alpha_{Med}$
NGC 6541	12.9	-1.82	14.44	0.16	0.26	0.73	$-0.75 \pm 0.16$	$-0.60 \pm 0.51$	$-1.17 \pm 0.22$
NGC 6544	11.1	-1.47	12.16	0.82	0.38	0.82	$-0.49 \pm 0.19$	—	$-0.46 \pm 0.26$
NGC 6558	12.3	-1.37	14.67	0.40	0.37	0.80	$+1.53 \pm 0.15$	—	$+1.49 \pm 0.16$
NGC 6584	12.0	-1.50	15.62	0.11	0.30	0.78	$-0.80 \pm 0.13$	$-0.61 \pm 0.13$	$-0.95 \pm 0.19$
NGC 6624	11.9	-0.42	14.52	0.27	0.28	0.82	$+0.66 \pm 0.16$	—	$+0.48 \pm 0.17$
NGC 6626	12.7	-1.46	13.64	0.49	0.19	0.78	$-0.18 \pm 0.18$	$-0.24 \pm 0.40$	$-0.31 \pm 0.19$
NGC 6637	11.8	-0.59	14.75	0.20	0.26	0.86	$+0.10 \pm 0.19$	—	$-0.13 \pm 0.29$
NGC 6638	12.0	-0.99	15.05	0.40	0.42	0.82	$+0.71 \pm 0.22$	—	$+0.71 \pm 0.22$
NGC 6642	12.7	-1.19	14.43	0.44	0.32	0.80	$+1.00 \pm 0.15$	—	$+0.87 \pm 0.18$
NGC 6652	11.9	-0.76	14.88	0.15	0.26	0.83	$+0.84 \pm 0.17$	$+1.11 \pm 0.51$	$+0.90 \pm 0.33$
NGC 6656	12.8	-1.70	12.66	0.39	0.18	0.74	$-0.90 \pm 0.15$	$-0.58 \pm 0.35$	$-1.22 \pm 0.25$
NGC 6681	13.0	-1.62	14.86	0.16	0.23	0.78	$-0.17 \pm 0.13$	$-0.41 \pm 0.45$	$+0.20 \pm 0.15$
NGC 6712	11.2	-1.02	14.24	0.55	0.35	0.84	$-0.24 \pm 0.17$	—	$-0.10 \pm 0.28$
NGC 6715	12.0	-1.44	17.15	0.16	0.52	0.80	$-1.43 \pm 0.19$	—	$-1.43 \pm 0.19$
NGC 6717	12.8	-1.26	14.38	0.23	0.30	0.79	$+1.47 \pm 0.18$	—	$+1.29 \pm 0.36$
NGC 6723	12.8	-1.10	14.54	0.11	0.23	0.79	$-0.33 \pm 0.14$	$-0.14 \pm 0.24$	$-0.58 \pm 0.21$
NGC 6752	12.8	-1.55	13.09	0.09	0.14	0.78	$-0.67 \pm 0.13$	$-0.61 \pm 0.27$	$-0.88 \pm 0.32$
NGC 6779	13.2	-2.00	15.19	0.25	0.31	0.77	$-0.56 \pm 0.15$	$-0.41 \pm 0.20$	$-0.84 \pm 0.18$
NGC 6809	13.3	-1.93	13.61	0.15	0.16	0.67	$-0.93 \pm 0.13$	$-0.81 \pm 0.16$	$-0.86 \pm 0.24$
NGC 6838	11.9	-0.82	13.01	0.28	0.25	0.82	$-0.17 \pm 0.15$	$-0.06 \pm 0.20$	$-0.80 \pm 0.30$
NGC 6934	12.0	-1.56	15.93	0.12	0.38	0.79	$-1.15 \pm 0.15$	—	$-1.26 \pm 0.15$
NGC 6981	11.9	-1.48	16.11	0.06	0.40	0.81	$-0.68 \pm 0.13$	—	$-0.68 \pm 0.13$
NGC 7006	12.2	-1.46	17.97	0.09	0.36	0.79	$-1.26 \pm 0.14$	—	$-1.52 \pm 0.16$
NGC 7078	13.0	-2.33	15.15	0.11	0.18	0.73	$-0.97 \pm 0.12$	$-0.57 \pm 0.28$	$-1.36 \pm 0.15$
NGC 7089	12.1	-1.66	15.44	0.06	0.24	0.78	$-0.87 \pm 0.16$	$-0.62 \pm 0.35$	$-1.17 \pm 0.19$
NGC 7099	13.1	-2.33	14.67	0.07	0.20	0.77	$-0.76 \pm 0.13$	$-0.73 \pm 0.16$	$-1.12 \pm 0.16$
Pal 1	7.6	-0.51	15.24	0.20	0.20	1.00	$-0.51 \pm 0.17$	$-0.04 \pm 0.34$	$-1.15 \pm 0.28$
Pal 5	11.1	-1.41	16.66	0.11	0.29	0.81	$-0.84 \pm 0.19$	$-0.39 \pm 0.44$	$-0.96 \pm 0.27$
Pal 12	9.3	-0.81	16.33	0.02	0.37	0.84	$-0.61 \pm 0.15$	—	$-0.76 \pm 0.19$
Pal 13	13.4	-1.78	16.70	0.18	0.24	0.78	$+0.29 \pm 0.22$	$+0.93 \pm 0.31$	$-0.12 \pm 0.40$
Pal 15	12.7	-2.10	18.22	0.45	0.47	0.78	$-1.41 \pm 0.16$	—	$-1.41 \pm 0.16$
Pyxis	11.2	-1.20	17.81	0.28	0.42	0.83	$-1.44 \pm 0.16$	—	$-1.44 \pm 0.16$
Rup 106	11.2	-1.78	16.58	0.20	0.22	0.81	$-0.81 \pm 0.14$	$-0.35 \pm 0.19$	$-1.11 \pm 0.15$
Sgr II	12.0	-2.28	18.92	0.22	0.45	0.80	$-1.51 \pm 0.17$	—	$-1.51 \pm 0.17$
Ter 7	7.3	-0.12	16.93	0.05	0.35	1.04	$-1.61 \pm 0.14$	—	$-1.85 \pm 0.16$
Ter 8	13.2	-2.16	17.20	0.16	0.28	0.77	$-1.14 \pm 0.15$	—	$-1.92 \pm 0.20$

**APPENDIX B: ADOPTED PARAMETERS AND  
DERIVED MASS FUNCTION SLOPES FOR  
THE CLUSTERS STUDIED IN THIS PAPER**

**APPENDIX C: SOURCES OF ADDITIONAL  
KINEMATIC DATA OF GLOBULAR CLUSTERS**

**Table B2.** Adopted parameters and derived mass function slopes for the LMC/SMC star clusters. The final column gives the mass function slope of the high-mass stars with  $m > 1 M_{\odot}$ . The meaning of the other columns is the same as in Table B1.

Cluster	log Age [yr]	[Fe/H]	Dist. mod.	E(B-V)	$m_{Low}$ [ $M_{\odot}$ ]	$m_{High}$ [ $M_{\odot}$ ]	$\alpha_{Tot}$	$\alpha_{Med}$	$\alpha_{High}$
Fornax 1	10.08	0.00	20.73	0.05	0.67	0.79	$-1.19 \pm 0.14$	$-1.18 \pm 0.14$	—
Fornax 3	10.08	-2.33	20.73	0.03	0.66	0.79	$-1.15 \pm 0.12$	$-1.15 \pm 0.20$	—
Hodge 6	9.40	-0.35	18.50	0.09	0.75	1.37	$-2.25 \pm 0.13$	$-1.39 \pm 0.22$	$-2.48 \pm 0.21$
Hodge 301	7.38	-0.30	18.50	0.10	1.28	6.26	$-2.36 \pm 0.24$	—	$-2.36 \pm 0.24$
Kron 3	9.81	-1.08	18.91	0.03	0.49	0.98	$-1.15 \pm 0.12$	$-1.15 \pm 0.12$	—
Lindsay 1	9.88	-1.14	18.78	0.06	0.48	0.94	$-1.19 \pm 0.14$	$-1.18 \pm 0.14$	—
Lindsay 38	9.81	-1.59	19.12	0.02	0.49	0.94	$-1.46 \pm 0.22$	$-1.47 \pm 0.22$	—
Lindsay 113	9.72	-1.44	18.80	0.00	0.54	0.99	$-0.80 \pm 0.19$	$-1.24 \pm 0.21$	—
NGC 121	10.02	-1.46	19.06	0.05	0.53	0.84	$-0.96 \pm 0.18$	$-1.16 \pm 0.18$	—
NGC 330	7.49	-0.98	18.90	0.07	0.78	6.96	$-2.38 \pm 0.25$	—	$-2.18 \pm 0.25$
NGC 339	9.78	-1.14	18.80	0.03	0.54	1.01	$-1.66 \pm 0.13$	$-1.66 \pm 0.13$	—
NGC 416	9.78	-1.00	18.91	0.08	0.59	0.99	$-1.46 \pm 0.21$	$-1.55 \pm 0.21$	—
NGC 419	9.18	-0.67	18.85	0.02	0.53	1.50	$-2.03 \pm 0.19$	$-2.03 \pm 0.22$	—
NGC 1651	9.30	-0.53	18.46	0.02	0.58	1.37	$-1.87 \pm 0.21$	$-1.21 \pm 0.15$	$-2.05 \pm 0.15$
NGC 1755	7.90	-0.50	18.35	0.13	0.91	5.27	$-2.37 \pm 0.27$	—	$-2.58 \pm 0.29$
NGC 1783	9.18	-0.35	18.46	0.02	0.63	1.51	$-1.93 \pm 0.19$	$-1.40 \pm 0.15$	$-2.53 \pm 0.15$
NGC 1806	9.18	-0.60	18.46	0.02	0.60	1.57	$-2.01 \pm 0.18$	—	$-2.44 \pm 0.21$
NGC 1846	9.18	-0.49	18.46	0.06	0.65	1.66	$-2.06 \pm 0.21$	—	$-2.21 \pm 0.23$
NGC 1850	8.00	-0.31	18.35	0.10	0.67	4.56	$-2.06 \pm 0.22$	—	$-2.16 \pm 0.25$
NGC 1856	8.54	-0.30	18.44	0.15	0.88	2.96	$-2.23 \pm 0.30$	—	$-2.35 \pm 0.35$
NGC 1866	8.23	-0.36	18.50	0.09	0.73	3.93	$-2.45 \pm 0.22$	—	$-2.14 \pm 0.24$
NGC 1978	9.30	-0.35	18.40	0.05	0.62	1.44	$-1.46 \pm 0.17$	$-1.10 \pm 0.17$	$-2.04 \pm 0.17$
NGC 2121	9.51	-0.50	18.30	0.10	0.69	1.19	$-2.19 \pm 0.29$	$-1.44 \pm 0.21$	—
NGC 2155	9.51	-0.46	18.30	0.03	0.77	1.21	$-0.60 \pm 0.53$	—	—
NGC 2173	9.20	-0.42	18.44	0.10	0.63	1.58	$-2.22 \pm 0.14$	—	—
NGC 2203	9.26	-0.41	18.41	0.12	0.60	1.50	$-1.41 \pm 0.16$	$-1.41 \pm 0.21$	—
R 136	6.20	-0.30	18.50	0.40	1.82	35.03	$-2.02 \pm 0.23$	—	$-2.02 \pm 0.23$
Reticulum	10.08	-1.66	18.39	0.05	0.42	0.80	$-1.28 \pm 0.16$	$-1.28 \pm 0.16$	—
SL 639	7.34	-0.30	18.50	0.35	1.83	8.23	$-2.48 \pm 0.26$	—	$-2.48 \pm 0.26$

**Table C1.** Sources of kinematic data on globular clusters used in this work in addition to Baumgardt (2017) and Baumgardt & Hilker (2018) (LOS = line-of-sight radial velocities, PM = proper motion velocity dispersions)

Name	Source	Type
NGC 104	Cerniauskas et al. (2018)	LOS
	Libralato et al. (2022)	PM
	Martens et al. (2023)	LOS
NGC 288	Ferraro et al. (2018)	LOS
	Libralato et al. (2022)	PM
NGC 362	Ferraro et al. (2018)	LOS
	Libralato et al. (2022)	PM
	Martens et al. (2023)	LOS
NGC 1261	Ferraro et al. (2018)	LOS
	Muñoz et al. (2021)	LOS
	Marino et al. (2021)	LOS
	Libralato et al. (2022)	PM
	Wan et al. (2023)	LOS
NGC 1851	Ferraro et al. (2018)	LOS
	Libralato et al. (2022)	PM
	Wan et al. (2023)	LOS
	Martens et al. (2023)	LOS
NGC 2298	Libralato et al. (2022)	PM
NGC 2808	Martens et al. (2023)	LOS
NGC 3201	Ferraro et al. (2018)	LOS
	Giesers et al. (2019)	LOS
	Wan et al. (2021)	LOS
	Libralato et al. (2022)	PM
	Martens et al. (2023)	LOS
NGC 4590	Libralato et al. (2022)	PM
	Wan et al. (2023)	LOS
NGC 4833	Libralato et al. (2022)	PM
NGC 5024	Libralato et al. (2022)	PM
	del Pino et al. (2022)	PM
NGC 5053	del Pino et al. (2022)	PM
NGC 5139	Johnson et al. (2020)	LOS
NGC 5272	Ferraro et al. (2018)	LOS
	Libralato et al. (2022)	PM
NGC 5286	Libralato et al. (2022)	PM
	Martens et al. (2023)	LOS
NGC 5466	Libralato et al. (2022)	PM
	del Pino et al. (2022)	PM
NGC 5897	Libralato et al. (2022)	PM
NGC 5904	Libralato et al. (2022)	PM
	Martens et al. (2023)	LOS
NGC 5927	Ferraro et al. (2018)	LOS
	Libralato et al. (2022)	PM
NGC 6093	Göttgens et al. (2021)	LOS
NGC 6101	Libralato et al. (2022)	PM
NGC 6121	Libralato et al. (2022)	PM
NGC 6171	Ferraro et al. (2018)	LOS
	Libralato et al. (2022)	PM
NGC 6205	Libralato et al. (2022)	PM
NGC 6218	Libralato et al. (2022)	PM
	Martens et al. (2023)	LOS
NGC 6254	Ferraro et al. (2018)	LOS
	Barth et al. (2020)	LOS
	Libralato et al. (2022)	PM
	Martens et al. (2023)	LOS

**Table C1 – continued**

Name	Source	Type
NGC 6266	Martens et al. (2023)	LOS
NGC 6293	Martens et al. (2023)	LOS
NGC 6304	Libralato et al. (2022)	PM
NGC 6341	Libralato et al. (2022)	PM
NGC 6342	Cohen et al. (2021)	PM
NGC 6352	Libralato et al. (2022)	PM
NGC 6355	Cohen et al. (2021)	PM
NGC 6362	Dalessandro et al. (2021)	LOS
	Libralato et al. (2022)	PM
NGC 6388	Libralato et al. (2022)	PM
	Martens et al. (2023)	LOS
NGC 6397	Libralato et al. (2022)	PM
	Martens et al. (2023)	LOS
NGC 6401	Cohen et al. (2021)	PM
NGC 6402	Johnson et al. (2019)	LOS
NGC 6496	Ferraro et al. (2018)	LOS
NGC 6535	Libralato et al. (2022)	PM
NGC 6541	Libralato et al. (2022)	PM
	Martens et al. (2023)	LOS
NGC 6558	Cohen et al. (2021)	PM
NGC 6584	Libralato et al. (2022)	PM
NGC 6624	Libralato et al. (2022)	PM
	Martens et al. (2023)	LOS
NGC 6637	Libralato et al. (2022)	PM
NGC 6642	Cohen et al. (2021)	PM
NGC 6652	Libralato et al. (2022)	PM
NGC 6656	Libralato et al. (2022)	PM
	Martens et al. (2023)	LOS
NGC 6681	Libralato et al. (2022)	PM
	Martens et al. (2023)	LOS
NGC 6715	Libralato et al. (2022)	PM
	Kacharov et al. (2022)	LOS
NGC 6717	Libralato et al. (2022)	PM
NGC 6723	Ferraro et al. (2018)	LOS
	Crestani et al. (2019)	LOS
	Libralato et al. (2022)	PM
	Taheri et al. (2022)	PM
NGC 6752	Libralato et al. (2022)	PM
	Martens et al. (2023)	LOS
NGC 6779	Libralato et al. (2022)	PM
NGC 6809	Rain et al. (2019)	LOS
	Libralato et al. (2022)	PM
NGC 6838	Barth et al. (2020)	LOS
	Libralato et al. (2022)	PM
NGC 6934	Marino et al. (2021)	LOS
	Libralato et al. (2022)	PM
NGC 7078	Kirby et al. (2020)	LOS
	Libralato et al. (2022)	PM
	Martens et al. (2023)	LOS
NGC 7089	Libralato et al. (2022)	PM
	Martens et al. (2023)	LOS
NGC 7099	Dalgleish et al. (2020)	LOS
	Libralato et al. (2022)	PM
	Martens et al. (2023)	LOS
Pal 15	Koch, Xu & Rich (2019)	LOS